Topographic and Mixed Layer Submesoscale Currents in the Near-Surface Southwestern Tropical Pacific

KAUSHIK SRINIVASAN, JAMES C. MCWILLIAMS, AND LIONEL RENAULT

Department of Atmospheric and Oceanic Sciences, University of California, Los Angeles, Los Angeles, California

HRISTINA G. HRISTOVA

Joint Institute for Marine and Atmospheric Research, University of Hawaii, Honolulu, Hawaii, and NOAA/Pacific Marine Environmental Laboratory, Seattle, Washington

JEROEN MOLEMAKER

Department of Atmospheric and Oceanic Sciences, University of California, Los Angeles, Los Angeles, California

WILLIAM S. KESSLER

NOAA/Pacific Marine Environmental Laboratory, Seattle, Washington

(Manuscript received 15 September 2016, in final form 28 January 2017)

ABSTRACT

The distribution and strength of submesoscale (SM) surface layer fronts and filaments generated through mixed layer baroclinic energy conversion and submesoscale coherent vortices (SCVs) generated by topographic drag are analyzed in numerical simulations of the near-surface southwestern Pacific, north of 16°S. In the Coral Sea a strong seasonal cycle in the surface heat flux leads to a winter SM ''soup'' consisting of baroclinic mixed layer eddies (MLEs), fronts, and filaments similar to those seen in other regions farther away from the equator. However, a strong wind stress seasonal cycle, largely in sync with the surface heat flux cycle, is also a source of SM processes. SM restratification fluxes show distinctive signatures corresponding to both surface cooling and wind stress. The winter peak in SM activity in the Coral Sea is not in phase with the summer dominance of the mesoscale eddy kinetic energy in the region, implying that local surface layer forcing effects are more important for SM generation than the nonlocal eddy deformation field. In the topographically complex Solomon and Bismarck Seas, a combination of equatorial proximity and boundary drag generates SCVs with large-vorticity Rossby numbers (Ro $\sim$ 10). River outflows in the Bismarck and Solomon Seas make a contribution to SM generation, although they are considerably weaker than the topographic effects. Mean to eddy kinetic energy conversions implicate barotropic instability in SM topographic wakes, with the strongest values seen north of the Vitiaz Strait along the coast of Papua New Guinea.

1. Introduction

Mesoscale eddies are prominent throughout the global ocean, with kinetic energies (KEs) that are typically about an order of magnitude larger than the mean kinetic energy (Stammer 1997; Chelton et al. 2011). The vertical and horizontal extent of these eddies scale with the thermocline depth and the thermocline baroclinic deformation radius R_d, respectively (Tulloch et al. 2011). Generated through baroclinic instability in the thermocline, and with typical midlatitude horizontal scales of around 50 km, these eddies have small Rossby (Ro = $U/fL \ll 1$) and Froude numbers (Fr = $U/HN \ll 1$) and are correspondingly geostrophically balanced. Here, U, L, and H are velocity, length, and depth scales of the mesoscale eddies, while f and N are the Coriolis parameter and associated buoyancy frequency. In certain regions, like the Coral Sea, mesoscale eddies can also be generated by barotropic instability of the nearly

NOAA/Pacific Marine Environmental Laboratory Contribution Number 4569 and Joint Institute for Marine and Atmospheric Research Contribution Number 16-394.

Corresponding author e-mail: Kaushik Srinivasan, kaushiks@atmos.ucla.edu

DOI: 10.1175/JPO-D-16-0216.1

zonal jets in the region (Qiu et al. 2009). Ageostrophic motions become significant and dynamically relevant at larger Rossby numbers (i.e., smaller length scales) and are often referred to as submesoscale currents or more concisely as submesoscales (SMs). A variety of routes to the generation of SM features have been identified in recent papers and typically occur at the ocean surface and bottom (Molemaker et al. 2015). Mixed layer instability (MLI; Boccaletti et al. 2007) of the weakly stratified surface mixed layer leads to the formation of mixed layer eddies (MLEs) and fronts (Fox-Kemper et al. 2008; Capet et al. 2008a) with horizontal scales ~10 km or less. MLEs are stronger for larger horizontal buoyancy gradients $\nabla_h b$ and deeper mixed layers H_b and are an important reason for the significant enhancement in SM activity during winter. Frontogenesis, originally identified in the context of the atmosphere (Hoskins and Bretherton 1972), occurs when the mesoscale eddy strain field enhances $\nabla_h b$ in the mixed layer through the action of a dynamically active ageostrophic secondary circulation, leading to the formation of fronts that can be clearly seen at the ocean surface in observations and models. While frontogenesis can occur independently from MLI, the two processes often accompany each other with secondary frontogenesis arising on the edges of MLEs. Furthermore, unlike the preceding inviscid mechanisms of SM generation and maintenance, a nonconservative SM process is associated with the secondary circulation and frontogenesis due to turbulent vertical momentum mixing in fronts and filaments (Gula et al. 2014; McWilliams et al. 2015), referred to as the turbulent thermal wind (TTW) balance. In general, all three dynamical processes are expected to be active in the surface layer, although their relative importance depends on the nature and strength of the (local) surface forcing and the (nonlocal) mesoscale eddy strain field. One of the aims of the present study is to examine the spatiotemporal evolution of mixed layer restratification fluxes and their dynamical attribution to the three SM processes discussed above in the southwestern tropical Pacific.

A different route to generating eddies, both mesoscale and SM, is the interaction of mean and mesoscale currents with topography. The basic mechanism [explained in Molemaker et al. (2015)] involves the boundary separation of high-vorticity sheets generated by bottom drag in the bottom boundary layers and subsequent barotropic or centrifugal instability that generates SM vortices and turbulence. The separated wakes have a ~0.1–10-km horizontal scale and roll up into either mesoscale or SM coherent vortices (SCVs), depending on whether the vortex Rossby number $\mathrm{Ro} = \zeta/f$ (where the vorticity $\zeta = \partial_x v - \partial_y u$) is small or $O(1)$. SCVs are gradient wind balanced (i.e., including the cyclostrophic force), as opposed to the usually geostrophically balanced mesoscale eddies. This is as much a dynamical definition of SM as it is one of scale (McWilliams 1985; Molemaker et al. 2015; Gula et al. 2015).

In this paper, we examine SM statistics and dynamics in the geographically diverse southwestern Pacific region north of 16°S (Fig. 1). The surface waters in the region are largely supplied by the westward flowing South Equatorial Current (SEC), which bifurcates at the coast of Australia into northward and southward western boundary currents. Somewhat uniquely, the northward western boundary current, the Gulf of Papua Current, is strongest subsurface (below 300 m) and remains so as it travels into the Solomon and Bismarck Seas. Before its bifurcation, the SEC waters form a series of alternating zonal jets in the Coral Sea by interacting with the islands chains of New Caledonia, Vanatu, and Fiji (Couvelard et al. 2008). Complex coastlines, island chains, and subsurface topographic features result in a high variability of the eddy kinetic energy (EKE) over seasonal (Hristova et al. 2014) and annual time scales (Kessler and Cravatte 2013; Melet et al. 2010). We show in this study that the interactions of the surface currents with topography are a significant source of SCVs in the Solomon and Bismarck Seas. Our focus is on SMs in the near-surface ocean (top 100 m).

Many recent papers have examined the southwestern Pacific using both observational and modeling approaches. Studies using mesoscale-resolving models and Argo and altimetry datasets have focused on seasonal and interannual variability in the Solomon Sea (Kessler and Cravatte 2013; Melet et al. 2010). These studies show that the upper ocean has an ENSO-like variability, since the Solomon Sea lies within the equatorial warm pool. Mesoscale eddies are the dominant variability on seasonal and subseasonal time scales, with anticyclones showing a weak dominance compared to the cyclones (Hristova et al. 2014). The maximum EKE in the Solomon Sea is distributed over all of its central region in agreement with satellite altimetry data (Hristova et al. 2014; Gourdeau et al. 2014). Djath et al. (2014) uses a submesoscale-permitting model of the Solomon Sea on a horizontal grid resolution of 1/36° (around $\Delta x = 3$ km) to study spectral properties of velocity in the Solomon Sea. They find a progressive shallowing of energy wavenumber spectral slopes with increasing resolution and the possibility of a forward kinetic energy cascade at small scales. In this study, we characterize the spatial structure, seasonal variability, and dynamics of SMs in the tropical southwestern Pacific region in and around the Solomon Sea. We use a hierarchy of nested, realistic geometry cases in the Regional Oceanic Modeling System (ROMS), with horizontal resolutions as

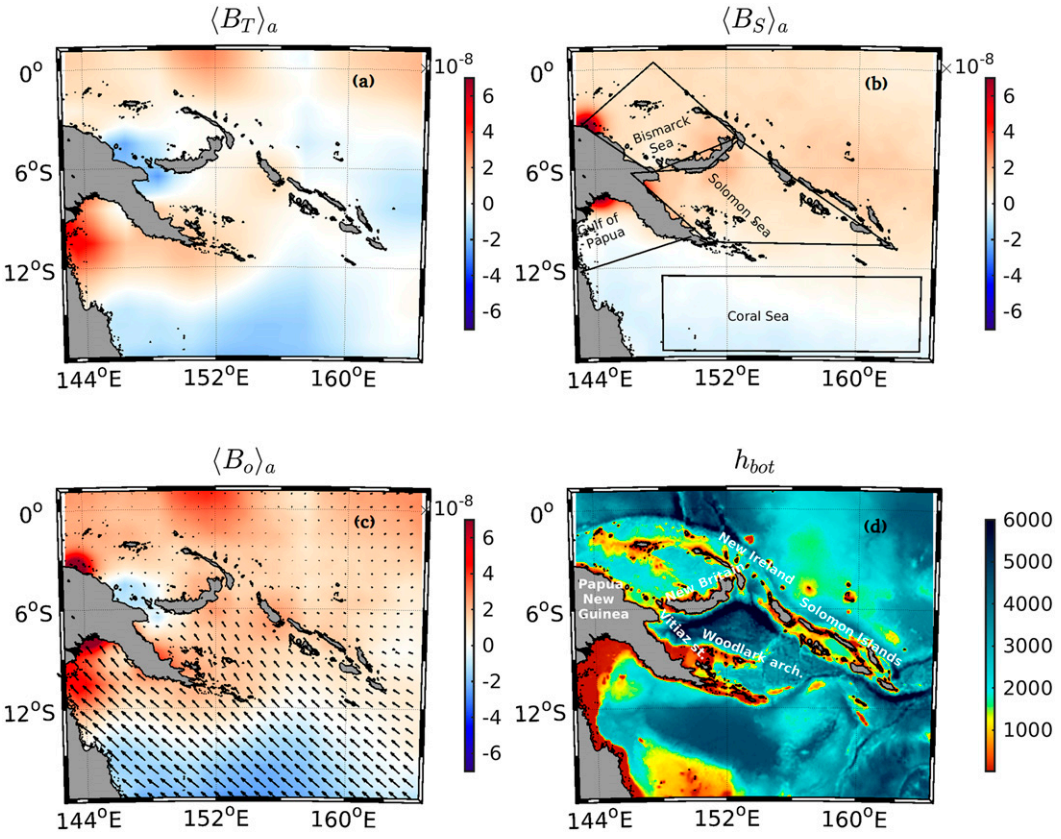

FIG. 1. Maps of the annually averaged surface fluxes ($m^2 s^{-3}$) of (a) heat, (b) freshwater, (c) buoyancy [with annually averaged wind stress ($N m^{-2}$) overlaid], and (d) the bottom topography in the region. Four analysis subdomains are indicated with black lines in (b): Bismarck Sea, Solomon Sea, Gulf of Papua, and Coral Sea.

fine as $\Delta x = 500$ m, to analyze SM behavior in several distinctive subregions of the southwestern Pacific. The paper is organized as follows: Section 2 describes the model details and numerical methodology. Section 3 characterizes the statistics of mesoscales and submesoscales in this region and their seasonal variability. In section 4, the SM dynamics is analyzed by looking at the spatiotemporal variability and vertical structure of the available potential energy (APE) conversion to SM kinetic energy (i.e., the restratification flux). This section also presents a comparison of this model-based restratification flux with existing theories and parameterizations for SM turbulence in the mixed layer. Section 5 examines the energetics of topography-induced submesoscale generation at the island chains and straits in and around the Solomon and Bismarck Seas, while the final section summarizes and concludes this manuscript.

2. Methodology

All the simulations are made using ROMS, a primitive equation, split–explicit, hydrostatic, terrain-following, σ-coordinate oceanic model (Shchepetkin and McWilliams 2003, 2005). Momentum advection is computed using a third-order, upwind-biased scheme (Shchepetkin and McWilliams 2005) that is the equivalent to a fourth-order central scheme supplemented by a biharmonic diffusion operator whose local diffusivity depends both on velocity and grid size Δx, such that it vanishes as $\Delta x \to 0$. Tracer advection is performed using an isoneutral advection scheme that helps preserve water mass properties (Lemarié et al. 2012).

a. Model cases

The simulations are computed using a set of nested ROMS cases starting from a case with $\Delta x = 12$ km that spans a decade in time and the entire Pacific Ocean. The boundary and initial conditions for this run are generated from SODA climatology (Carton and Giese 2008). A nested $\Delta x = 4$ km case is then computed for the region between the latitudes of 40°S and 10°N and the longitudes 130°E and 160°W. The boundary and initial conditions are constructed from the 12-km output fields using the methodology explained in Mason et al. (2010).

The $\Delta x = 4$ km case has also been the subject of a recent analysis of the mesoscale structure and variability in this region (Hristova et al. 2014). Employing a similar methodology, a $\Delta x = 1.5$ km case is computed for a period spanning a year, and it can be considered to be "submesoscale permitting" in the sense that at least the larger SM eddies and fronts are resolved. The spinup time in both cases is just over 3 months, and the model data during that period are excluded from the analyses presented here. The vertical grid structure in all three cases of the hierarchy is identical and consists of $N = 51\sigma$ levels. Our highest-resolution run, a $\Delta x = 500$ m case, nested down from $\Delta x = 1.5$ km spans the winter months of June, July, and August and has $N = 100\sigma$ levels. The $\Delta x = 500$ m run is, however, only used marginally in the present paper and will be a subject of future studies, with a majority of the results here based on the $\Delta x = 1.5$ km run. The vertical grid stretching is done with the parameters $\theta_s = 6$, $\theta_b = 1.5$, and $h_c = 250$ m [for an explanation of the ROMS vertical grid structure, see Shchepetkin and McWilliams (2009)]. The ocean surface and bottom are parameterized using the K-profile parameterization (Large et al. 1994), which has seen widespread use in ocean and climate models (Danabasoglu et al. 2006). Its precise formulation in ROMS differs from Large et al. (1994) in determining the boundary layer depth h_{BL} with an integral functional composed of the stratification, shear, rotation, and turbulent buoyancy flux influences (McWilliams and Huckle 2006; McWilliams et al. 2009; Lemarié et al. 2012). This approach, explained in detail in Lemarié et al. (2012), alleviates some of the computational oscillations potentially present, leading to improved spatial smoothness.

b. Surface wind stress and buoyancy forcing

The surface wind stress and heat and freshwater fluxes are constructed using the approach detailed in Lemarié et al. (2012). This is done with a two-step procedure. The first step is used to generate a wind stress climatology, and the second step is to add its daily variability. The climatology is the QuikSCAT-based Scatterometer Climatology of Ocean Winds (SCOW) for the years 2004–09, corrected using buoy data from the Tropical Atmosphere–Ocean Array in the equatorial Pacific. The daily variability is obtained from the Centre ERS d'Archivage et de Traitement (CERSAT; French ERS processing and archiving facility) wind anomalies for the period July 2005 to June 2006 with an adjustment to ensure periodicity in time for this interval. Thus, a single, year-long, periodic, daily wind product is obtained and then repeated to generate multiyear forcing. The present simulations are therefore idealized process studies, in the sense that interannual variability is excluded from the atmospheric forcing, but intraseasonal forcing is allowed. The surface heat fluxes are obtained from the 1° Common Ocean–Ice Experiment (CORE) monthly climatology over the period 1981–2006, supplemented with a weak restoring toward a Pathfinder SST climatology. The freshwater fluxes are obtained from Hamburg Ocean Atmosphere Parameters and Fluxes from Satellite Data (HOAPS-3) climatology over the period 1987–2005 at ½° resolution with a weak restoring toward the *World Ocean Atlas 2005* climatology. The river runoff is simulated as a surface precipitation, spatially spread around the river mouth. The annual-averaged heat and salinity fluxes are shown in Fig. 1, expressed as contribution to the surface buoyancy flux B_o, where buoyancy is rescaled density $b = -g\rho'/\rho_0$. The flux B_o is related to the surface heat Q and freshwater [evaporation − precipitation $(E - P)$] fluxes by

$$B_o = \underbrace{g\alpha Q_o/(\rho_0 C_p)}_{B_T} - \underbrace{g\beta(E-P)S}_{-B_S}. \qquad (1)$$

In Fig. 1b, there is a net freshwater flux north of 12°S and in the river mouths north and south of Papua New Guinea. The seasonal winter cooling in the Coral Sea is also prominently visible. Even though the annual averages seem to imply comparable contributions from the heat flux and the net freshwater flux, we see in Fig. 2 that the variability in the B_T is up to a factor of 3 greater than in B_S, indicating that the intraseasonal variations might be dominated by temperature, a fact that is confirmed in section 4b. The Gulf of Papua has the weakest winter cooling signal, with strong surface heating and freshwater outflows at the river mouths. The spatially averaged B_S seasonal cycle in Fig. 2 includes contributions from both riverine outflows and surface $(E - P)$ forcing. While the total annual freshwater input in the Solomon Sea is largely due to the surface precipitation term P in the Bismarck Sea and Gulf of Papua regions, river outflows have significant contributions. The total annual riverine output into the Gulf of Papua is comparable to other river systems; in particular, it is about half of the Mississippi river outflow. Surface precipitation in the Solomon and Bismarck subdomains account for most of the B_S with a smaller fraction accounted for by the riverine outflows. The seasonal variability of the wind stress, τ and its standard deviation are also shown in Fig. 2. The mean wind stress varies contemporaneously with the surface heat flux, reflecting the atmospheric Hadley circulation. In general, within the spatial extent of the $\Delta x = 1.5$ km case, the mean surface wind stress increases with increasing latitude.

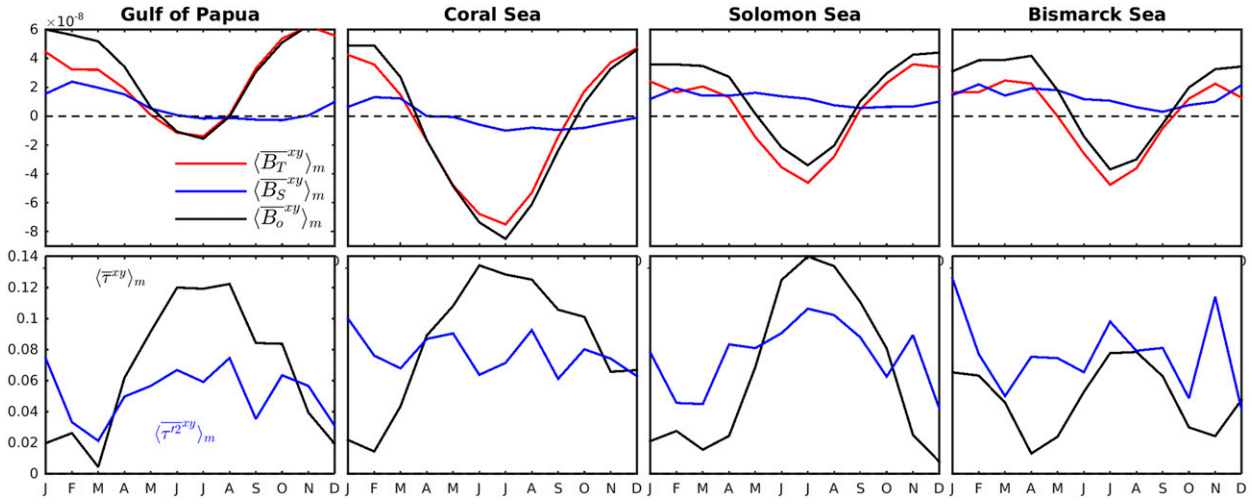

FIG. 2. (top) Seasonal cycle of spatially averaged surface fluxes of heat, freshwater, and buoyancy ($m^2 s^{-3}$). (bottom) Seasonal cycle of spatially averaged surface wind stress $\langle \overline{\tau}^{xy} \rangle_m$ and its standard deviation $\langle \overline{\tau'^2}^{xy} \rangle_m^{1/2}$ ($N m^{-2}$). The spatial averaging is performed over the four regions delineated in Fig. 1.

The choice of the spatial averaging subdomains in Fig. 1 is somewhat arbitrary. The Coral Sea is a simple choice, bereft of near-surface topographic effects or freshwater fluxes. A prominent seasonal cycle in wind and buoyancy fluxes allows a careful examination of mixed layer SMs. The Gulf of Papua subdomain is chosen to study the role of freshwater forcing and associated fronts. The Solomon and Bismarck subdomains examine the effects of equatorial proximity on SM currents. In section 5, a different set of near-boundary averaging regions is chosen to specifically examine the relative influence of topographic and mixed layer generation of SMs.

The spatiotemporal averages in this paper are the following: Temporal averaging is performed over monthly $\langle \cdot \rangle_m$, seasonal $\langle \cdot \rangle_s$, or annual time scales $\langle \cdot \rangle_a$. Spatial averaging operators are written as $\overline{(\cdot)}^{xy}$, with the region of averaging typically being one of the four choices in Fig. 1, while volume averages $\overline{(\cdot)}^{xyz}$ include the depth dimension with the range between the surface and the base of the mixed layer.

3. Mesoscale and submesoscale statistics

Figure 3 shows a snapshot of surface vorticity based on simulations collated from the three nested cases in the Southern Hemisphere winter season (in this paper all seasons are relative to the Southern Hemisphere). The surface vorticity patterns of the 4-km case are dominated by eddies, but higher-resolution cases also prominently display SM frontal patterns. A distinct pattern of reduced magnitude of vorticity is seen on approaching the equator (where geostrophic balance is weaker). Next we analyze the spatiotemporal statistics of the surface vorticity, horizontal velocity divergence, buoyancy gradient, and frontogenetic tendency, quantities that are associated with SM fronts and filaments (Capet et al. 2008b). The EKE, which is dominated by the mesoscale eddy field and is the subject of numerous previous studies, is also briefly discussed.

a. Eddy kinetic energy

The annual cycle and dynamics of mesoscale eddies has been previously analyzed by Hristova et al. (2014) using the same $\Delta x = 4$ km model case used here. It shows good agreement between the geostrophic EKE in the model compared to satellite altimetry measurements. Here, we briefly compare the EKE from the previously analyzed 4-km case with the $\Delta x = 1.5$ km case. The EKE here is computed from velocity anomalies derived relative to a climatological monthly mean. In Fig. 4, we see that the mesoscale variability in the Solomon Sea displays similar spatial patterns and magnitudes, in spite of the shorter time of averaging (hence greater estimation error) in the $\Delta x = 1.5$ km case, implying a degree of convergence of EKE estimate with model resolution. This is because the mesoscale eddies and boundary current fluctuations dominate the EKE, unlike most of the other quantities examined in the subsequent subsections that are dominated by SM variability. Some differences do arise in the spatial patterns of EKE in the Coral Sea, however, although the magnitudes are of a similar order. In fact, EKE values averaged over each year of the $\Delta x = 4$ km case in the Coral Sea have differences with the same order of magnitude and spatial structure as seen between the $\Delta x = 4$ and 1.5 km cases

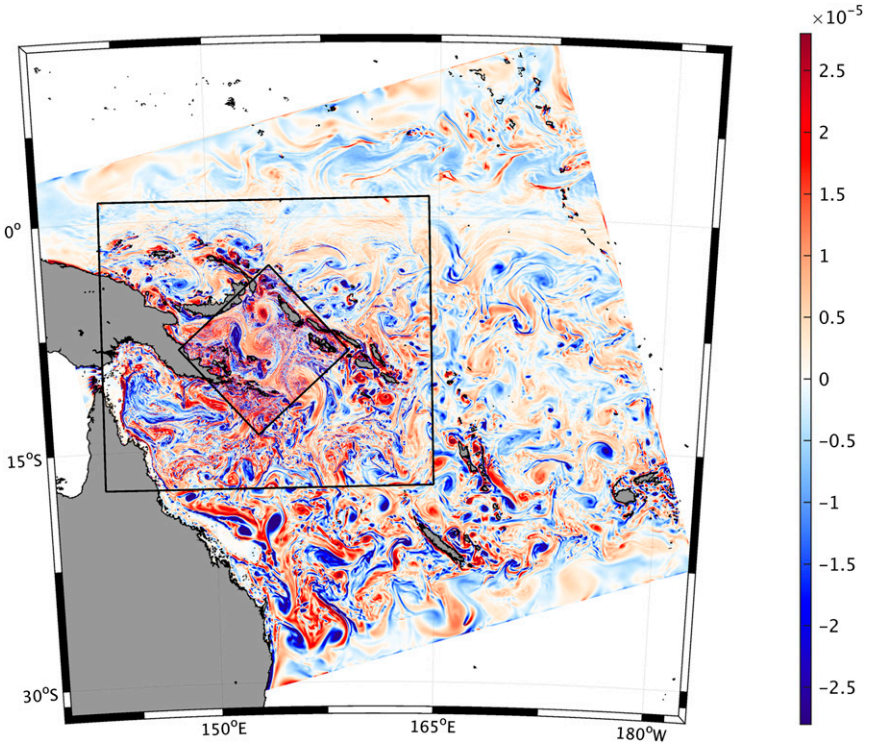

FIG. 3. A snapshot of the magnitude of surface vertical vorticity ζ (s^{-1}) from the nested ROMS hierarchy of $\Delta x = 4$, 1.5, and 0.5 km cases. Their respective domains are outlined by black boxes. The date of the snapshot is 1 Jun.

(not shown). This is not a serious impediment to our study of SM currents, which are much smaller than mesoscale eddies and have much shorter lifetimes (typically a few days compared to a few weeks for mesoscale eddies), thereby allowing more accurate SM statistical estimations.

In a previous study of the Coral Sea mesoscales, Qiu et al. (2009) attributes the EKE in a latitudinal band 14°–18°S as caused by barotropic instability of the alternating zonal current system (the North Vanatu jet–Coral Sea Countercurrent–New Caledonia jet Current System) in this region. Using a reduced gravity shallow water model that compares well with the results from satellite altimetry, they find an EKE peak in the months of December–January (DJ) and a minimum in May–June (MJ). Our analysis of the EKE seasonal cycle in

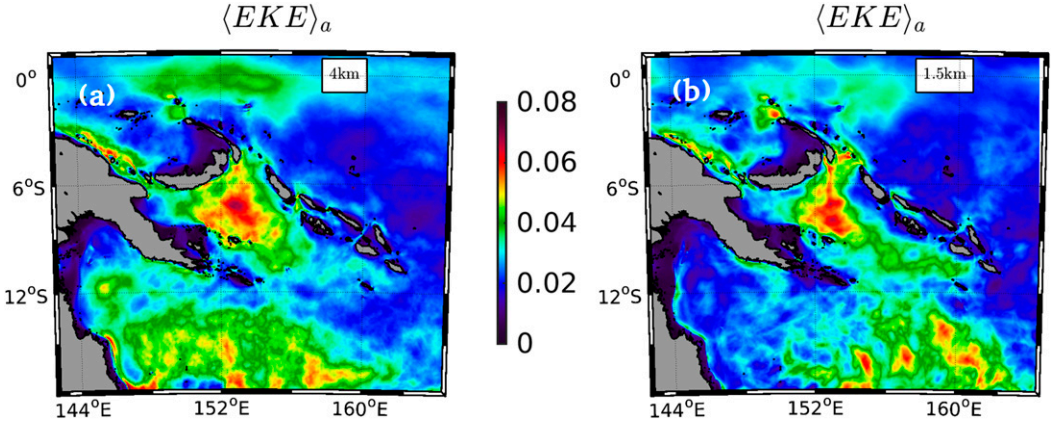

FIG. 4. Spatial patterns of the annually averaged surface EKE ($m^2 s^{-2}$) in and around the Solomon Sea from the $\Delta x =$ (a) 4 and (b) 1.5 km cases.

this latitude band leads to similar results (not shown). In sum, the EKE variation in the region is out of phase with the seasonal local surface forcing of wind and buoyancy flux (Fig. 2), raising the intriguing question of whether the nonlocal forcing (the mesoscale eddy deformation field) or the local surface forcing is more important for SM generation. Below we show that local forcing effects typically dominate, mirroring previous studies of midlatitude SM seasonal cycles (e.g., Mensa et al. 2013) that lack the strong mesoscale seasonal cycle observed in this region.

b. Vertical velocity and vorticity

The quasigeostrophic (QG) equations have a fundamental cyclone–anticyclone symmetry ($\zeta \leftrightarrow -\zeta$) that is approximately validated in observed (Chelton et al. 2011) and modeled (Tulloch et al. 2011) analyses of mesoscale eddies. QG mesoscale eddies also have a relatively weak vertical velocity w, solely because of the deflection of isopycnals over the spatial scale of the pycnocline baroclinic deformation radius R_d ($\approx$50 km in the midlatitudes and even larger in the tropics). Recent studies (Callies et al. 2015; Chavanne and Klein 2016) using mixed layer QG models predict the emergence of MLEs with a size much smaller than R_d, associated with the somewhat less clearly defined (owing to ambiguities in defining the surface layer stratification) mixed layer deformation radius $R_{\rm ml}$ [$R_{\rm ml} = \sqrt{H_b \Delta b_{\rm ml}}/f \approx O(1)$ km] in midlatitudes. The associated vertical velocity is correspondingly much larger than in thermocline QG models, but in QG models it has an upwelling–downwelling ($w \leftrightarrow -w$) symmetry concomitant with the $\zeta \leftrightarrow -\zeta$ symmetry. The QG dynamics is formally invalid when Ro ~ 1, which can happen when the strain field generated by mesoscale and MLEs rapidly increases the existing $\nabla_h b$ to large values (provided $\nabla_h b$ has a nonzero projection on the direction of local principal strain), leading to the formation of fronts and filaments. One of the dynamical mechanisms for frontogenesis involves an O(Ro) ageostrophic secondary circulation in the cross-frontal plane generated by the strain field, which has an upwelling, anticyclonic, lighter side and a downwelling, cyclonic, heavier side. On the two sides, cyclonic vorticity is enhanced and anticyclonic vorticity is diminished by the vortex stretching and compression in the vorticity relation

$$\frac{D\zeta}{Dt} \approx (f + \zeta)\frac{\partial w}{\partial z}. \tag{2}$$

In addition, because of the finite Ro asymmetry, the downwelling w on the cyclonic side is larger in a front than the upwelling on the lighter side. The TTW balance in fronts and filaments similarly exhibits a secondary circulation that leads to cyclonic and downwelling dominance (McWilliams et al. 2015; Gula et al. 2014). Thus, the near-surface w, the surface horizontal divergence $\delta = \partial_x u + \partial_y v$, and ζ are expected to have finite skewness in regions of active SM frontal dynamics.

We compute temporal statistics for the model cases (with instantaneous output files available twice a day) at each point in our domain. Spatial maps of these temporal statistics for the summer [January–March (JFM)] and winter [July–September (JAS)] season are presented in Figs. 5 and 6. The skewness statistic is masked, subject to a variance constraint skew$[\langle \delta'^2 \rangle < C] = 0$, where $C = 3 \times 10^{-11}\,{\rm s}^{-2}$, with a similar criterion used to mask the vorticity skewness. This focuses attention on regions with appreciable SM variability.

1) Coral Sea submesoscale "soup"

The largest seasonal contrast is in the statistics for both ζ and δ in the Coral Sea. This is indicative of a strong SM activity in the winter (Fig. 3), with the large skewness in ζ and δ demonstrating clear cyclonic and downwelling dominance. Similar seasonal cycles have been found in midlatitude simulations (Mensa et al. 2013; Gula et al. 2014) and observations (Callies et al. 2015). Previous studies have largely interpreted the seasonal SM as being a consequence of MLEs, but we show in section 3d that frontogenesis and TTW processes are also consistent with this seasonal cycle. The primary reason for this SM seasonality is that the surface wind stress and surface heat flux, which control the boundary layer mixing and H_b, also have a strong seasonal cycle (Fig. 2). The Coral Sea panels of Fig. 7 underscore these results: the statistical indicators of SM activity are clearly stronger in the $\Delta x = 1.5$ km case. Perhaps more interestingly, there is small temporal phase difference in the peak values of both δ and ζ variance between the cases: the $\Delta x = 1.5$ km case has its peak activity in July–August as opposed to September for the 4-km case.

2) Bismarck and Solomon Seas topographic submesoscales

In contrast to the open Coral Sea, large δ and ζ variance values are seen along the eastern coasts of Papua New Guinea and New Ireland (Fig. 5) in the west Solomon Sea off the Woodlark Archipelago and generally along island wakes visible as coastally spun eddies and fronts in the snapshots in Figs. 3 and 8. These are a result of the separation of bottom drag–generated shear layers in shallow water that spawn near-surface SM eddies. They are especially prevalent near coastal headlands and islands with strong passing currents, for

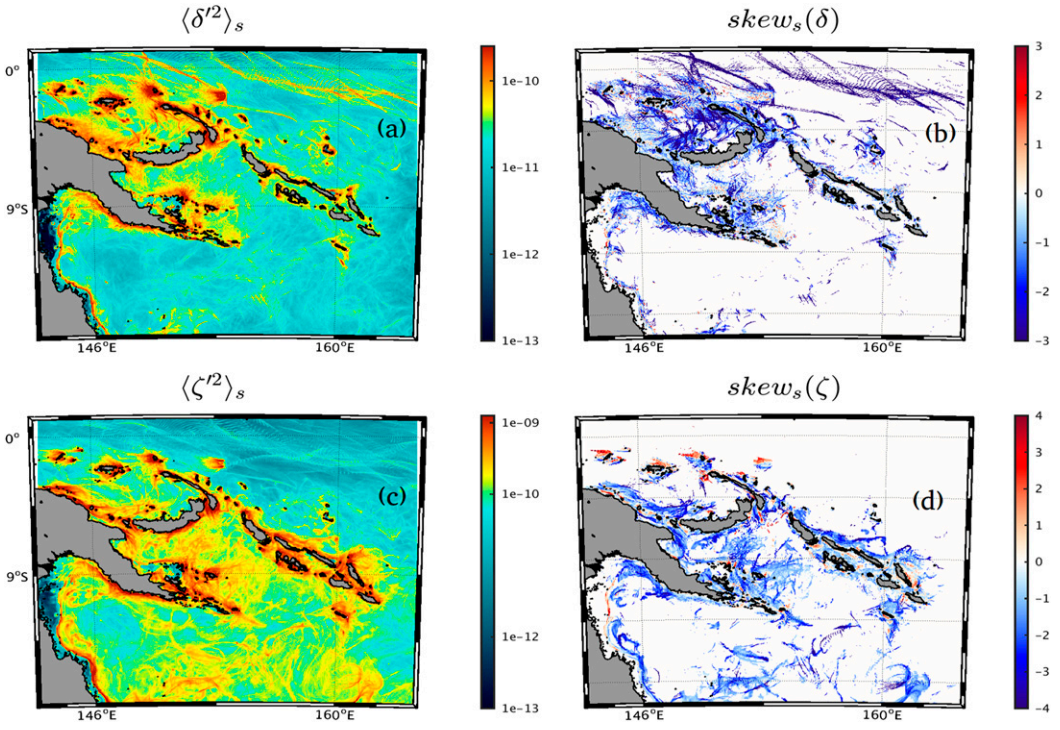

FIG. 5. Spatial patterns of the rms variability of surface horizontal divergence δ' and vertical vorticity ζ' (s^{-1}) and their associated skewness computed over the summer months of January, February, and March in and around the Solomon Sea from the $\Delta x = 1.5$ km case. The skewness calculation is spatially masked (white space) using a variance threshold to avoid regions of weak variability.

example, the northward flow during the winter through the relatively Vitiaz Strait and the SEC along the eastern coast of New Ireland. The equatorial proximity and small island sizes off the Vitiaz Strait and New Ireland ensure that the eddy generation involves SM dynamics with rather large Rossby numbers ~10 (Dong and McWilliams 2007).

The skew(ζ) values in the winter island wakes implicate anticyclonic generation (red patches in Fig. 5), consistent with the sign of vorticity generated by northwestward currents flowing along these coasts. Similar anticyclonic SCVs have been studied in detail by Molemaker et al. (2015) off the California coast due to California Undercurrent separation off a headland. The summer months also show smaller but significant SCVs in the Bismarck Sea and off the eastern Papua New Guinea coast and in some of the island wakes surrounding the Solomon Sea. These are principally topography related (boundary generated and consistent with the wind stress seasonal cycle), but off the eastern Papua New Guinea coast itself, some generation can be attributed to freshwater-generated fronts off the river mouths. Such fronts were recently shown to be of dynamical importance off the coast of the (more voluminous) Mississippi River in the Gulf of Mexico (Luo et al. 2016). As we show in section 3c, freshwater-induced fronts do occur in this region but are strongest between the months of February to May, which do not have significant local maxima in the right panels of Fig. 7.

A higher-resolution ($\Delta x = 500$ m) Solomon Sea case during the winter season (Fig. 9) has, as expected, a much stronger SM signal relative to the $\Delta x = 1.5$ km case. As with the $\Delta x = 1.5$ km case, the $\Delta x = 500$ m SM features are dominated by eddies and fronts generated through interaction of mesoscale flow with the topographic features off the Woodlark Archipelago and the Solomon Islands to the east (not shown). What is significant, however, is a strong signature of secondary frontal instabilities and internal waves in the $\Delta x = 500$ m case that are poorly resolved in the $\Delta x = 1.5$ km case (not shown). These features are notably absent in midlatitude simulations of comparable resolution (e.g., Gula et al. 2014). One reason for this is that the larger baroclinic deformation radius (≈200 km) and the mixed layer deformation radius (≈5 km) in the Solomon Sea, compared to the midlatitudes at the same grid resolution, has higher effective resolution, owing to equatorial proximity. However, because this paper is a broad study of SMs in this region, a detailed dynamical description of the $\Delta x = 500$ m case is deferred to future studies, and the

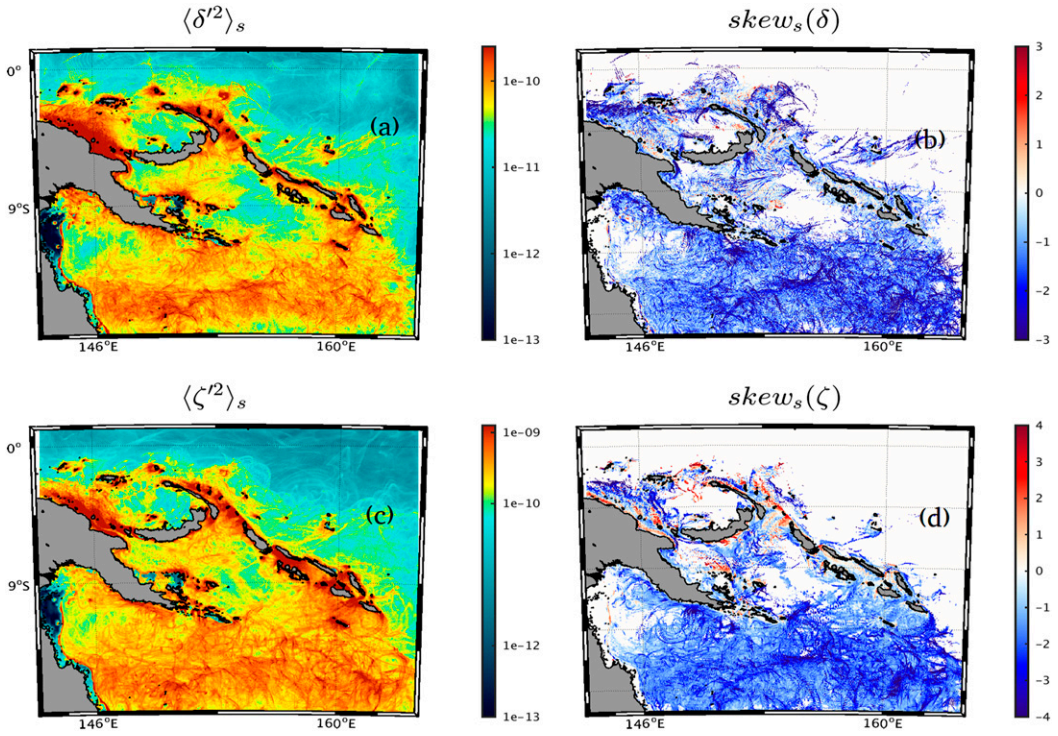

FIG. 6. As in Fig. 5, but for the months of June, July, and August.

SM statistics and dynamics shown in this paper are largely derived from the $\Delta x = 1.5$ km case.

3) THE EAST SOLOMON SEA SUBMESOSCALE "DESERT"

A persistent feature of the statistical maps in Figs. 5 and 13 (below) is the weakness of SM signatures in the eastern Solomon Sea, year-round. This is in spite of the large EKE signal (Fig. 4) associated with the presence of large mesoscale eddies in the region, seen, for example, in maps of the vorticity averaged over the month of November (the choice of November is arbitrary with similar eddies seen all year; Fig. 10; $R_d \approx 200$ km at this latitude). Three large and persistent mesoscale eddies are seen during this month, with weak values of buoyancy gradient and frontogenetic tendency in the eddy centers. This is consistent with the results in Capet et al. (2008a,b) that eddy centers typically have strong vorticity values and weak values of strain and $|\nabla_h b|$, while the opposite happens near the eddy boundaries where SM processes are most active. Thus, the mesoscale strain field is conducive to fronts and frontogenesis at the eddy

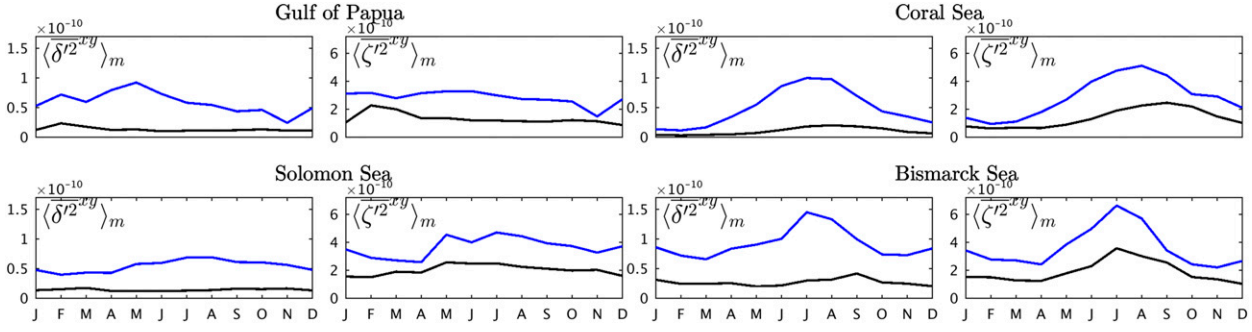

FIG. 7. Seasonal cycle of surface δ and ζ variance (s^{-2}) averaged over the four regions for the $\Delta x = 4$ (black) and 1.5 km (blue) cases. Notice the strong increase in these SM indicators with resolution. See Fig. 9 for comparison with the $\Delta x = 500$ m case during the winter months.

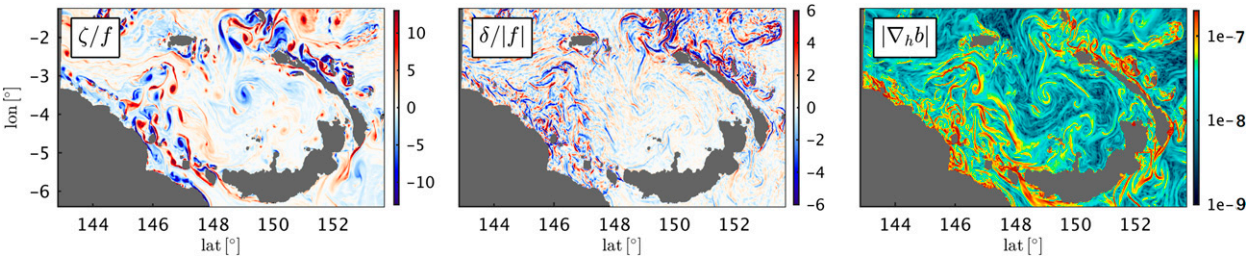

FIG. 8. Snapshots of surface ζ/f, $\delta/|f|$, and $|\nabla_h b|$ (s^{-2}) in the Bismarck Sea on 1 Jul from the $\Delta x = 1.5$ km case. Note that July is the month of peak SM variance in this region (see Fig. 7).

edges. While these maps only depict the month of November, similar large eddies are usually prevalent in the eastern Solomon Sea and give rise to the SM desert seen in the statistical maps of Figs. 5 and 13. An alternative approach to characterizing the relative influences of vorticity and strain is through the Okubo–Weiss parameter $Q = \zeta^2 - S^2$, where $S^2 = (u_x - v_y)^2 + (u_y + v_x)^2$ is the trace of the strain tensor. In a submesoscale-permitting study in the tropical North Atlantic, Veneziani et al. (2014) find that the equatorial regions are dominated by strain $Q < 0$, similar to the situation in the Solomon Sea, resulting in weaker frontogenesis.

4) LATITUDINAL VARIATION OF SUBMESOSCALE STATISTICS

In Fig. 3, a general decrease of both mesoscale eddies and SM fronts, away from the boundaries, was seen on approaching the equator. This is qualitatively expected because the mechanisms of baroclinic instability and frontogenesis both require rotation. A quantitative view of the decrease of SM amplitudes as a function of latitude is displayed in Fig. 11 for the month of June by examining zonally averaged statistics of previously discussed SM proxies. To allow for a relative comparison of their latitudinal variability, we normalize each zonally averaged statistic with their maximum values over the domain. [Thus, we are plotting $\langle|\overline{\nabla_h b}|^x\rangle_m/\max(\langle|\overline{\nabla_h b}|^x\rangle_m)$ and so on.] Then by selectively masking out the near-boundary regions (i.e., within 90 km of the boundary) before zonal averaging (Fig. 11a) and comparing with the unmasked zonal averages (Fig. 11b), we find that in this region the SMs in the near-equatorial regions are primarily due to topographic effects. Thus, north of about 6°S, the SM generation mechanism can be thought to transition from mixed layer to topographic on approaching the equatorial region.

c. *Frontogenetic tendency*

Fronts are formed when horizontal density gradients are enhanced by various dynamical processes that include mesoscale strain, MLEs, and TTW-induced secondary circulations (section 1). From the buoyancy equation, the Lagrangian frontogenetic tendency can be written as

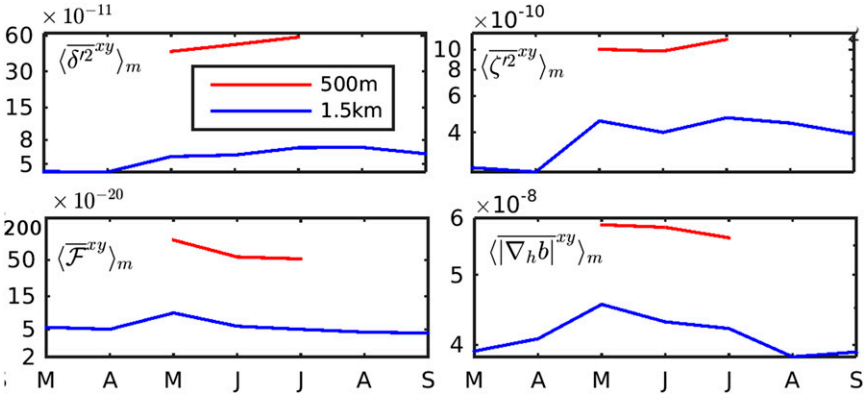

FIG. 9. Seasonal cycle of monthly mean values of surface δ'^2 (s^{-2}), ζ'^2 (s^{-2}), $\mathcal{F}$ (s^{-5}), and $\nabla_h b$ (s^{-2}) averaged over the Solomon Sea area for the $\Delta x = 1.5$ km (blue) and 500 m (red) cases. The $\Delta x = 500$ m case is only available during the winter months.

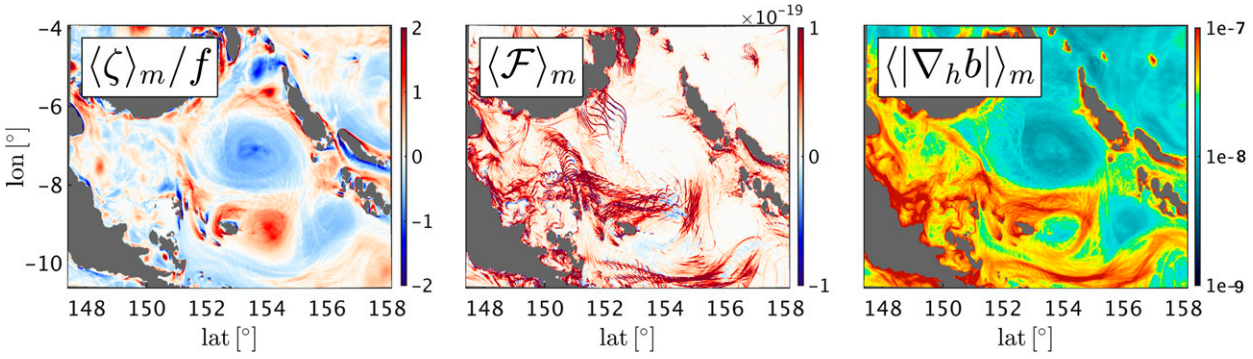

FIG. 10. Maps of surface $\langle\zeta\rangle_m/f$, $\langle\mathscr{F}\rangle_m$ (s^{-5}; section 3c), and $\langle|\nabla_h b|\rangle_m$ (s^{-2}) in the Solomon Sea, averaged over the month of November for the $\Delta x = 1.5$ km case.

$$\frac{D|\nabla_h b|^2}{Dt} = \mathscr{F}, \tag{3}$$

where $\mathscr{F}$ is the frontogenetic tendency consisting of advective, vertical mixing, and horizontally diffusive terms (Capet et al. 2008b). The diffusive and mixing terms are generally frontolytic (i.e., $\mathscr{F} < 0$), although the latter has a more complex effect for the case of TTW fronts and filaments (Gula et al. 2014). Fronts and filaments are typically formed when the advective part is frontogenetic ($\mathscr{F} > 0$), and this component is defined as $\mathscr{F} = \mathbf{Q} \cdot \nabla_h b$, where

$$\mathbf{Q} = -(\partial_x u \partial_x b + \partial_x v \partial_y b, \partial_y u \partial_x b + \partial_y v \partial_y b). \tag{4}$$

We construct temporal averages of $|\nabla_h b|$ and $\mathscr{F}$ in a manner similar to the δ and ζ statistics in section 3b. In both these quantities the SM components dominate. The dominance of frontogenesis over frontolysis is evident in the probability distribution function (PDF) of surface $\mathscr{F}$

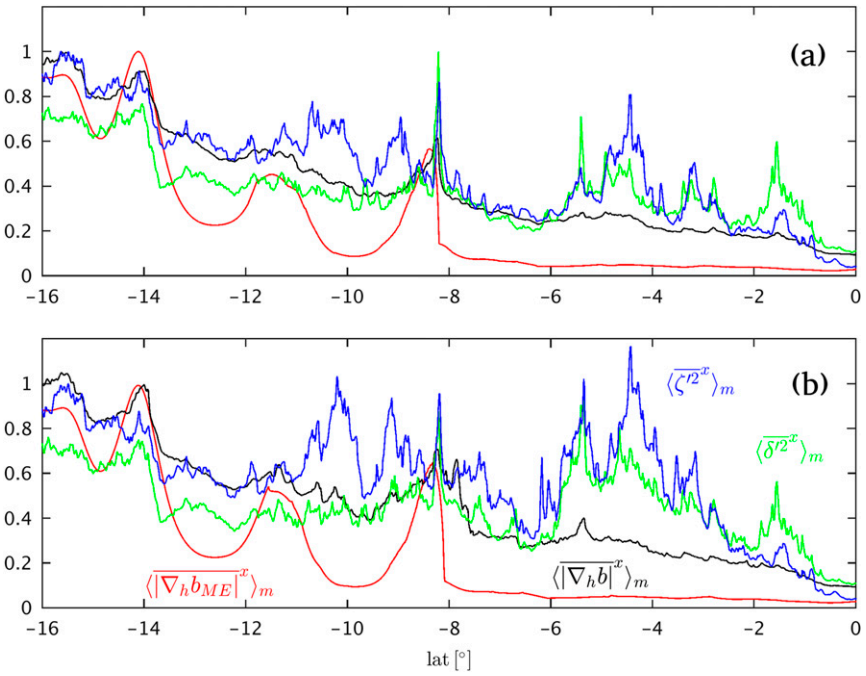

FIG. 11. Latitudinal variation of normalized [see section 3b(4) text for details], zonally averaged quantities averaged over the month of June at the surface. (a) The mesoscale filtered fields for buoyancy gradient $\langle\overline{|\nabla_h b_{ME}|}^x\rangle_m$ and the total field $\langle\overline{|\nabla_h b|}^x\rangle_m$ (s^{-2}) and the analogous vorticity quantities $\langle\overline{\zeta'^2}^x\rangle_m$ and $\langle\overline{\delta'^2}^x\rangle_m$ (s^{-2}), where regions within 90 km of the boundary are masked out before zonal averaging. (b) As in (a), but with zonal averaging performed over the entire domain without masking the boundary regions. These are for the $\Delta x = 1.5$ km case.

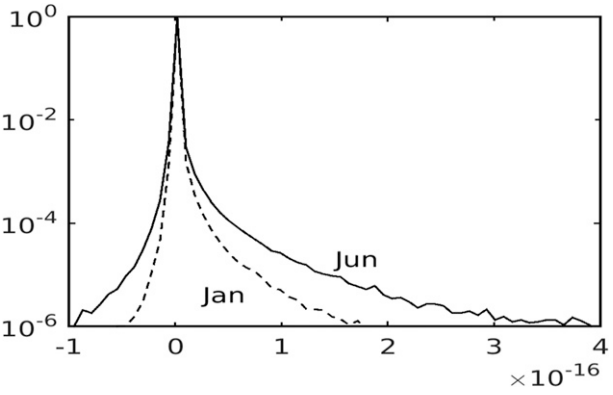

FIG. 12. Single-point PDF of surface frontogenetic tendency $\mathscr{F}(s^{-5})$ in the Coral Sea averaged over the months of January (dashed) and June (solid) in the subdomain indicated in Fig. 1. The associated skewness values are 154 and 175, respectively, that is, highly frontogenetic.

in the Coral Sea (Fig. 12). For the months of January and June, the PDFs have a strong positive skewness (≈150). The summer and winter maps in Fig. 13 show a winter enhancement in the Coral Sea soup, the coastal areas of the Bismarck Sea, and the Gulf of Papua. The spatial patterns in Figs. 13 and 5 are strikingly similar, and this confirms the link between a dynamically active ageostrophic secondary circulation (diagnosed by δ), frontogenesis, and frontal strength. Similar results are found in earlier studies (Capet et al. 2008b), although lacking the clear statistical picture provided here.

The regional seasonal cycles of the vertical structure of $\langle\mathscr{F}\rangle$ in Fig. 14 are somewhat challenging to interpret. The Coral Sea cycle shows a winter enhancement, as expected, from the deeper H_b values associated with the effects of wind stress and surface cooling (section 2b). The Gulf of Papua has a big $\langle\mathscr{F}\rangle$ signal corresponding to the season of strongest river outflows, owing to freshwater fronts clearly visible in Fig. 13. The Solomon and Bismarck Sea results are explained less easily; they have a vertical structure that is strongest just above the base of the mixed layer rather than throughout the surface layer or with surface intensification. In the maps of $\langle\mathscr{F}\rangle$ (Fig. 13), the large values occur near topographic SM source regions; the strongest is near the Vitiaz Strait, the coast of New Ireland, and the Woodlark Archipelago in the Solomon Sea. These large values are absent away from topography. We infer that the explanation of the unusual vertical structure must come from the topographic generation process in some way not yet known. In the Bismarck Sea, freshwater fronts do contribute to the $\mathscr{F}$ vertical structure because the river outflows are maximized in the season between February and May, but the strongest values seen between May and August are topography generated.

The role of freshwater forcing in generating SMs is subtle because in the open ocean it would be represented by a positive buoyancy forcing ($B_S > 0$), which if equated to the effects of surface heating ($B_S < 0$) would result in shallower mixed layers, reducing the APE reservoir [(5)] and thereby suppressing SM mixed layer

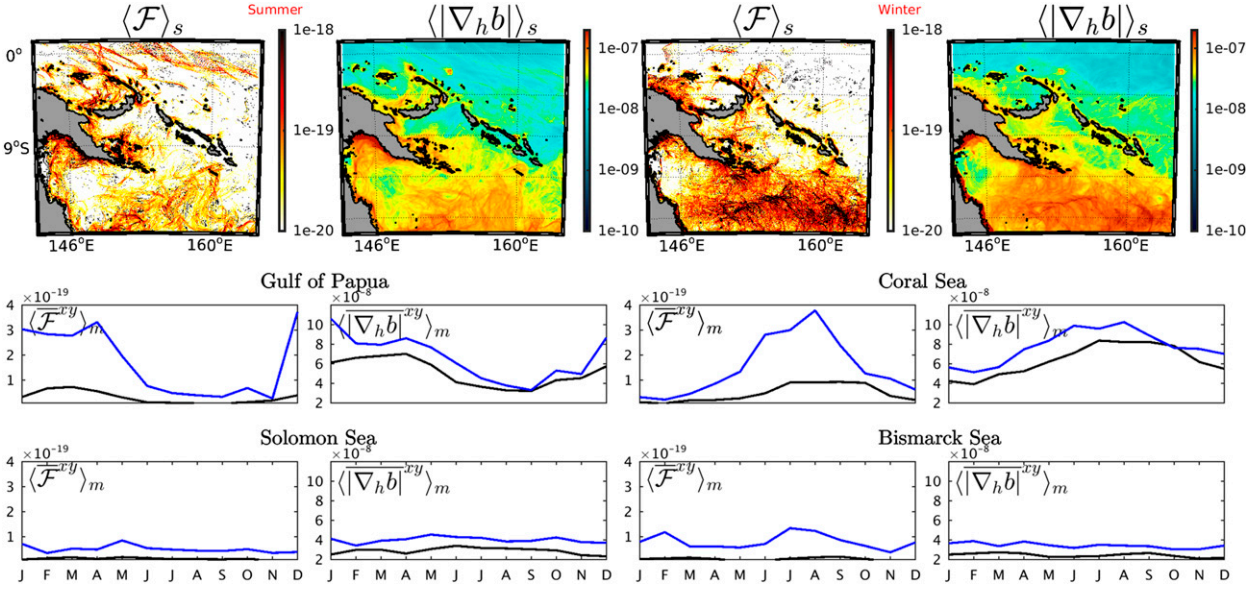

FIG. 13. (top) Maps of surface $\mathscr{F}(s^{-5})$ and $|\nabla_h b|$ (s^{-2}), temporally averaged over the (left) summer (JFM) and (right) winter (JJA) seasons over the southwestern Pacific region. (bottom) Seasonal cycle of surface $\mathscr{F}$ and $|\nabla_h b|$ averaged over the subdomains defined in Fig. 1. These are from the case with $\Delta x = 1.5$ km.

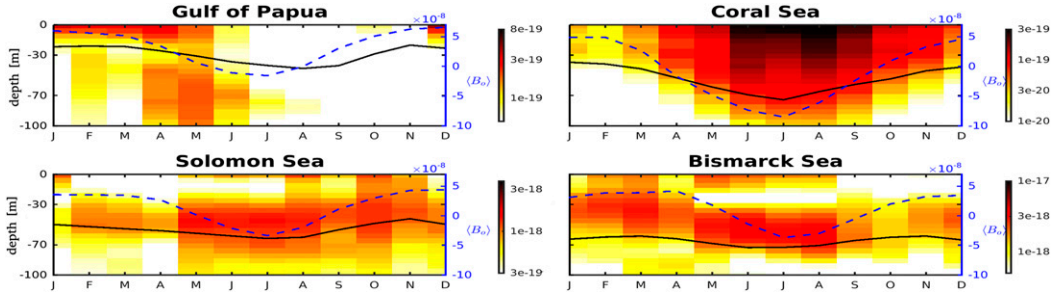

FIG. 14. Seasonal cycle of the frontogenetic tendency $\langle \overline{\mathscr{F}}^{xy} \rangle$ (s^{-5}), with spatial averaging performed over the indicated subdomains, from the $\Delta x = 1.5$ km run. Locations with depths shallower than 200 m are excluded. For comparison, the associated surface buoyancy flux $\langle B_o \rangle$ is also plotted (blue dashed line) along with H_b (black line).

generation. However, localized river outflows add fresh (and sometimes cool, like the Mississippi River) water into a saltier (and warmer) ocean creating large salinity and density fronts. Figure 13 highlights riverine frontogenesis in the form of enhanced values of $\langle \overline{\mathscr{F}}^{xy} \rangle_m$ and $\langle |\overline{\nabla_h b}|^{xy} \rangle_m$ in the Gulf of Papua, and to a lesser extent in the Bismarck region, from January to April when the riverine output is largest. In fact, the freshwater frontal gradients are as strong as those generated in the winter SM soup in the Coral Sea region. Our results mirror the findings of Luo et al. (2016) for the Mississippi River even though the total annual output there is roughly twice the Gulf of Papua river outflows. Figure 15 illustrates the impact of freshwater outflows at the ocean surface of this region for the month of April with strong values of $\langle |\nabla_h b| \rangle_m$ and $\langle \mathscr{F} \rangle_m$. Incidentally, while the Gulf of Papua rivers flow into the shallow shelf regions (like the Mississippi), the rivers to the north do not (Fig. 1).

4. Mixed layer submesoscale processes

a. Mixed layer depth and APE

The mixed layer depth H_b is diagnosed using the standard approach of the depth at which the temperature is 0.2°C below that at the surface. The depth H_b is principally determined by three physical processes: 1) the surface buoyancy flux that causes convective mixing-induced deepening or shallowing depending on the sign of the flux, 2) turbulent boundary layer mixing (that would in general also include surface wave effects) parameterized here by KPP, and 3) restratification fluxes induced by SM processes. Couvelard et al. (2015) attempts to quantify the impact of the SM fronts and eddies on H_b in an idealized baroclinic jet subjected to a winter cooling period. By varying their model resolution from an eddy-resolving $\Delta x = 10$ km to a SM-permitting $\Delta x = 2$ km, they find that the latter case had significantly shallower H_b because of stronger restratification fluxes that are absent in the former case. Similar results are found in the present study with generally shallower H_b values found in the $\Delta x = 1.5$ km case relative to the $\Delta x = 4$ km case (Fig. 16). During the winter months, H_b in the Solomon Sea (the green curve) is shallower, and the shallowing in the $\Delta x = 500$ m case is particularly dramatic compared to the lower-resolution cases by a factor of about 2. The Couvelard et al. (2015) study, however, lacks wind stress and a corresponding parameterized turbulent mixing that can have also have a significant SM imprint (Nagai et al. 2006). Idealized studies show that mixing can enhance MLE-induced restratification

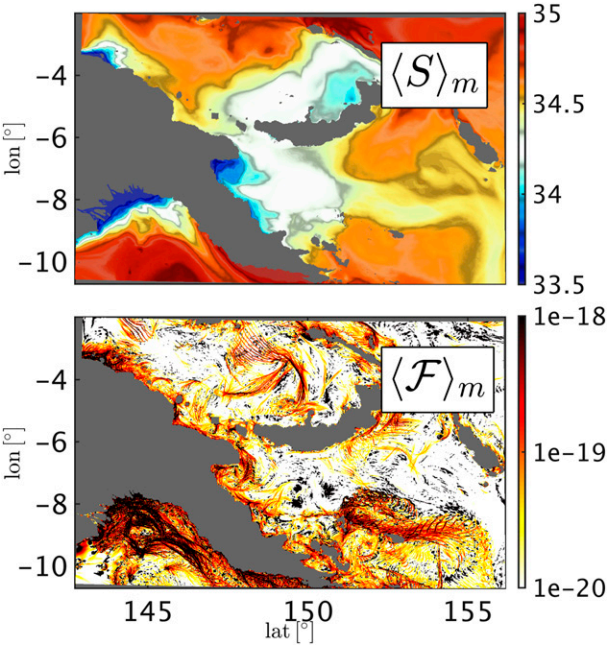

FIG. 15. Maps of S (psu) and frontogenetic tendency $\mathscr{F}$ (s^{-5}) averaged over the month of April (the month of peak river outflow in the Gulf), from the $\Delta x = 1.5$ km run.

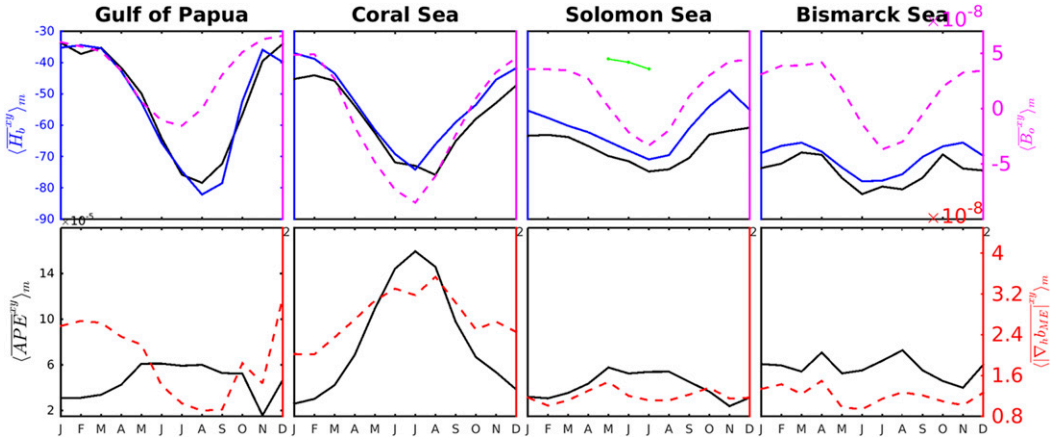

FIG. 16. (top) Seasonal cycle of the mixed layer depth H_b (m) in the $\Delta x = 4$ (black) and 1.5-km (blue) cases, along with B_o ($m^2 s^{-3}$) (magenta dashed) for comparison. The $\Delta x = 500$ m Solomon Sea case is also plotted (green) for the winter months. (bottom) APE from (5) ($m^2 s^{-2}$; black) and the mesoscale magnitude of the buoyancy gradient $|\nabla b_{ME}|$ (s^{-2}; dashed red).

(Bachman and Taylor 2016) and allow the formation of TTW fronts and filaments, which also restratify the surface layer (McWilliams et al. 2015; McWilliams 2016). Because the seasonal cycles of τ and B_o are so tightly coupled in the tropics, it can be difficult to decouple their relative effects on H_b variability and associated SMs (more on this in section 3d). Contrary to the discussion above, in previous studies H_b has been found to be the strongest determinant of the strength of restratification fluxes and their seasonal variability, both in idealized models (Brannigan et al. 2015; Couvelard et al. 2015) and the Gulf Stream region (Mensa et al. 2013). These results can be understood in the context of the mesoscale eddy APE reservoir available to energize SM currents, estimated under assumption of a vertically uniform surface buoyancy layer (Fox-Kemper et al. 2008; Brannigan et al. 2015) as

$$\mathrm{APE} \approx \frac{1}{2} H_b^2 \overline{|\nabla_h b_{\mathrm{ME}}|}^{z}, \tag{5}$$

where b_{ME} is the mesoscale component calculated with a spatial low-pass filter whose filter scale is close to R_d, and the depth average is computed over the mixed layer. Note that R_d increases rapidly close to the equator and a single filter choice for all latitudes risks corrupting the mesoscale signal with the SM $\nabla_h b$ values, which can have large local values due to frontogenesis. We pick the filter scale to be $L_f = 90$ km, somewhat less than the R_d value of 100 km in the Coral Sea, keeping in mind that lower-latitude values could include some of the SM $\nabla_h b$.

The seasonal variability of APE is plotted in Fig. 16 for the four regions. The Coral Sea APE has a strong winter maximum in line with the statistical measures of SMs in earlier sections. Interestingly, the $|\nabla_h b_{\mathrm{ME}}|$ signal here also has a broad winter maximum at odds with the EKE summer maximum detailed in Qiu et al. (2009) and briefly discussed in section 3a. This is not inconsistent with geostrophy because mesoscale eddies have a thermocline-scale thermal wind balance and not an H_b-scale balance. The Gulf of Papua region has a prominent February–April maximum in $|\nabla_h b_{\mathrm{ME}}|$, owing to strong river outflows. However, the seasonal cycle of H_b in the Gulf of Papua is out of phase with that of $|\nabla_h b_{\mathrm{ME}}|$, ensuring a broad winter maximum in APE because APE $\propto H_b^2$ is the stronger dependence. Thus, in spite of the large surface frontogenesis signal found in Fig. 13, shallower mixed layers, caused by strong surface heating (Fig. 2), reduce the total APE associated with the riverine output. This has obvious implications for the restratification flux.

b. *Vertical buoyancy fluxes and restratification*

The vertical eddy buoyancy flux (VBF), averaged over the mixed layer, represents a transfer of APE to KE near the surface:

$$\mathrm{APE} \rightarrow \mathrm{KE} = \frac{1}{H_b} \int \mathrm{VBF}(z)\, dz, \quad \mathrm{VBF} = \langle \overline{w' b'}^{xy} \rangle_m . \tag{6}$$

Turbulent convection induced by surface cooling would have negative values (represented as a subgrid-scale process in the ROMS model by KPP), while restratifying SM dynamics that arise from baroclinic conversion (section 1) have positive values (Boccaletti et al. 2007; Fox-Kemper et al. 2008; Capet et al. 2008b). Figure 17 shows the seasonal cycle of vertical structure of the

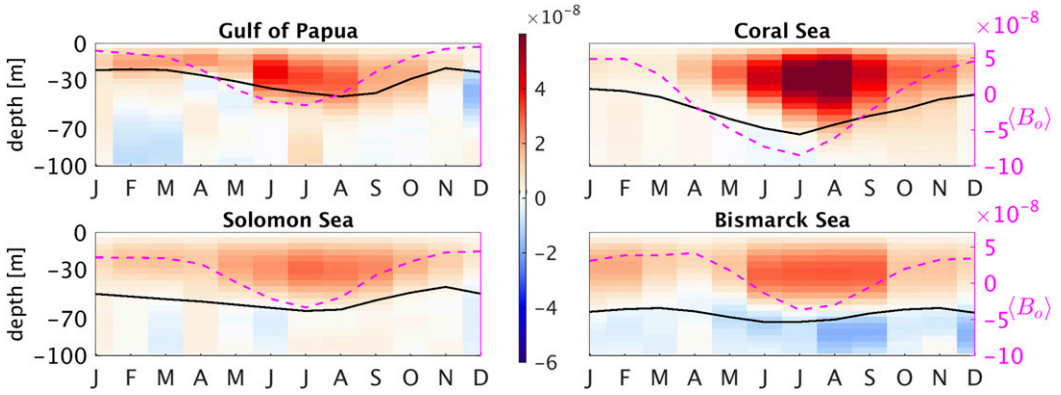

FIG. 17. Seasonal cycle of the vertical buoyancy fluxes VBF(z) ($m^2 s^{-3}$), with horizontal averaging over the indicated subdomains. For comparison, the associated surface flux $\langle B_o \rangle$ is plotted (purple) along with H_b (black).

spatially averaged VBF in the four subdomains. In general, VBF is restratifying and leads to a shallowing of H_b; notice in Fig. 16 the shallower values with higher resolution, leading to a bigger SM VBF.

The Coral Sea displays a clear winter maxima corresponding to the seasonal cycles of B_o and τ. The Bismarck and Solomon Seas have weaker seasonal cycles, with the Bismarck Sea in particular showing summer and spring restratification that coincides with the freshwater forcing from the river outflows and the usual (but weaker) surface cooling in the winter months. Further, as discussed in section 3b(2), the SM eddies in the Bismarck Sea are mainly coastally and topographically generated. Gula et al. (2015) analyzed SM generation in the wake of Gulf Stream separation off the Florida Straits and found that the dominant SM energy conversion was from the mean to eddy kinetic energy through the horizontal Reynolds stress:

$$\mathrm{HRS} = \overline{u'v'}\,\overline{u}_y + \text{similar terms}, \tag{7}$$

and not VBF. Our results mirror those of Gula et al. (2015), but we defer this discussion to section 5.

The Gulf of Papua has a VBF that is at its maximum during the winter months of May–July (MJJ) and not February–April (FMA), which corresponds to the season of strong surface frontogenesis (Fig. 13). The APE seasonal cycle for this region, estimated in the previous section, is therefore a better predictor of the VBF than the surface $\langle \overline{\mathscr{F}}^{xy} \rangle$ seasonal cycle, supporting the dependence of VBF on H_b. Further, fronts in shallower mixed layers have weaker, associated vertical velocity, again resulting in reduced VBF. Strong summer riverine frontogenesis and weak accompanying VBF was found in the Mississippi River outflow region of the Gulf of Mexico by Luo et al. (2016) using a ROMS-based model study, suggesting a similar dynamical mechanism in the two cases.

c. *T and S contributions to the VBF*

Seawater density depends nonlinearly on temperature T, salinity S, and pressure p. However, in the tropical surface layer it is sufficient to approximate it by a linear equation of state

$$b - b_0 = \alpha g(T - T_0) - \beta g(S - S_0), \tag{8}$$

where b_0, S_0, and T_0 are regional reference values, and α and β are regional constants for the expansion coefficients. The VBF can therefore be decomposed as

$$\overline{w'b'} = \underbrace{\overline{g\alpha w'T'}}_{\mathrm{VTF}} - \underbrace{\overline{g\beta w'S'}}_{-\mathrm{VSF}}, \tag{9}$$

where the averaging operator can include both temporal and spatial averages. Figures 18 and 19 display the individual contributions from T [i.e., vertical temperature flux (VTF) = $\overline{g\alpha w'T'}$] and S [i.e., vertical salinity flux (VSF) = $\overline{-g\beta w'S'}$] to the VBF. In most regions, the seasonal patterns of VSF and VBF are significantly different. Some of these differences can be related to local forcing effects. The Bismarck and Solomon regions, for example, have an expected winter maximum in VTF and a FMA maximum in VSF, reflecting the season of maximum riverine outflow. The Coral Sea also has a June–August (JJA) maximum that accounts for the VBF signal during this season. However, the VSF is largest during June and smaller at other times, despite lacking localized freshwater sources during this month ($B_S \approx 0$). To understand this result, consider the time-averaged equilibrium scalar balance equations for T and S:

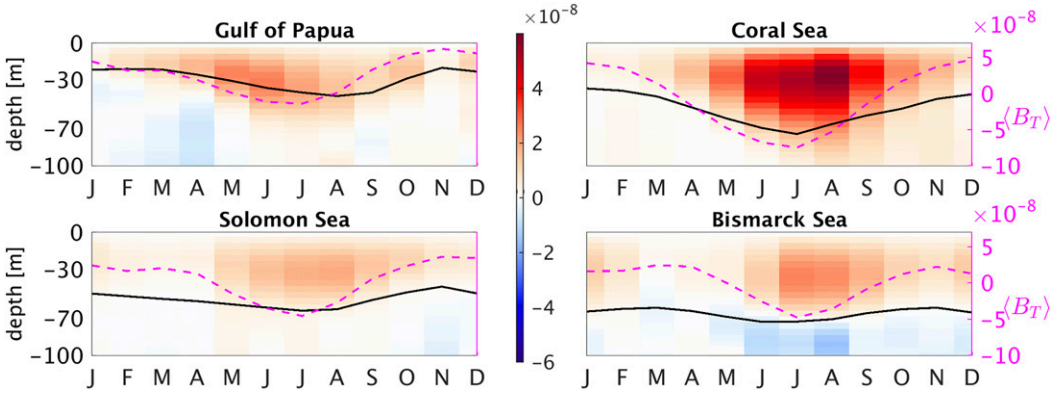

FIG. 18. Seasonal cycle of the vertical temperature flux $\mathrm{VTF}(z) = \langle \overline{g\alpha w' T'}^{xy} \rangle_m$ ($\mathrm{m^2\,s^{-3}}$), averaged over the indicated subdomains. For comparison, the associated surface flux $\langle B_T \rangle$ is plotted (purple) along with H_b (black).

$$\nabla \cdot \langle \mathbf{u}_h \{T, S\} \rangle_m + \partial_z \langle w \{T, S\} \rangle_m = \partial_z \langle \kappa \partial_z \{T, S\} \rangle_m, \quad (10)$$

where $\mathbf{u}_h = (\mathrm{u}, \upsilon)$ is the horizontal velocity, and κ is the KPP-supplied diffusivity. A similar equation is true for buoyancy because of the linear approximation in (8). The horizontal scalar fluxes are dominated by mesoscale eddies while the vertical fluxes are dominated by SM processes. The dominant SM balances are between the vertical advection term on the left side and the mixing term on the right side (Capet et al. 2008a).

On spatially averaging over the subdomains in Fig. 1 and integrating between the surface ($z = 0$) and mixed layer depth ($z = -H_b$), we get

$$\langle \overline{w' T'}^{xy} \rangle_m \approx \langle \kappa \partial_z \overline{T}^{xy} \rangle_m - \langle \overline{B_T / g\alpha} \rangle_m, \quad \text{and} \quad (11)$$

$$\langle \overline{w' S'}^{xy} \rangle_m \approx \langle \kappa \partial_z \overline{S}^{xy} \rangle_m + \langle \overline{B_S / g\beta} \rangle_m. \quad (12)$$

Thus, when $B_S \approx 0$, as in the Coral Sea during the winter months, then $\langle \overline{w' S'}^{xy} \rangle_m \approx \langle \kappa \partial_z \overline{S}^{xy} \rangle_m$, and consequently $\mathrm{VSF} \propto u^*$ due to $\kappa \propto u^*$ in a wind-driven regime with KPP. This analysis is consistent with the coincidence of the seasonal maxima in VSF and τ in the Coral Sea. We hypothesize that this is an example of SM generation by vertical boundary layer mixing induced by wind stress through TTW fronts and filaments (McWilliams et al. 2015) and MLEs in a TTW balance (Bachman and Taylor 2016). Actual justification of this hypothesis would require a careful analysis of the dynamical balance in the surface layer because the lowest-order balance of TTW fronts involves the vertical mixing term. For now, we merely note that the restratification flux due to TTW fronts [see (20) and the discussion surrounding it] has the form

$$\overline{w' b'}_{\mathrm{TTW}} \propto u^*, \quad (13)$$

and a local maximum in wind stress could lead to a local maximum in VBF (through VSF), consistent with the results in Figs. 19 and 17.

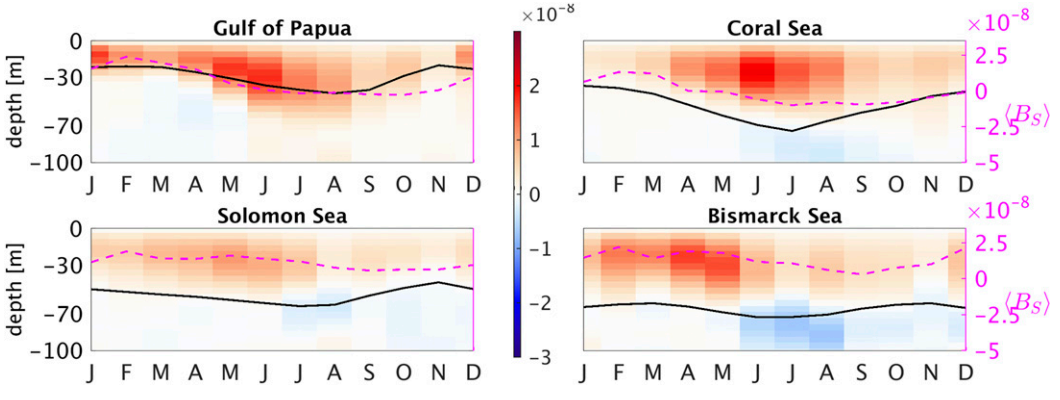

FIG. 19. Seasonal cycle of the vertical salinity flux $\mathrm{VSF}(z) = \langle \overline{-g\beta w' S'}^{xy} \rangle_m$ ($\mathrm{m^2\,s^{-3}}$), averaged over the indicated subdomains. For comparison, the associated surface flux $\langle B_S \rangle$ is plotted (purple) along with H_b (black). Notice that the color bar and B_S axis ranges are exactly half of the corresponding values in Figs. 17 and 18.

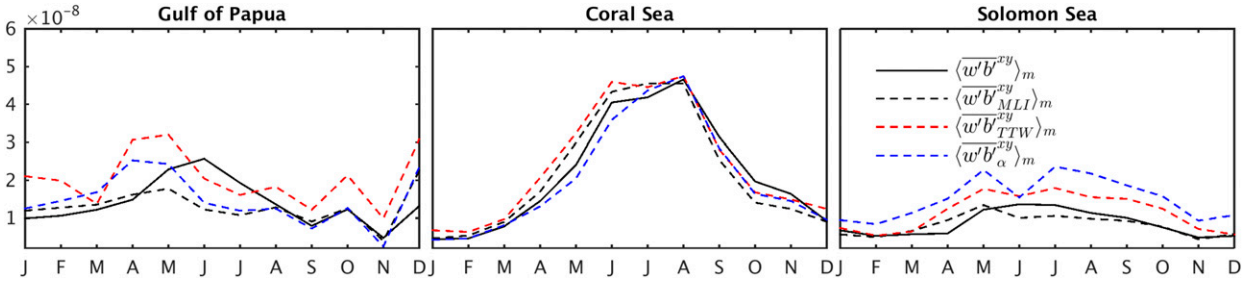

FIG. 20. Seasonal cycle of VBF, compared with the scale estimates from MLE $\overline{w'b'_{\mathrm{MLE}}}$, TTW $\overline{w'b'_{\mathrm{TTW}}}$, and α frontogenesis $\overline{w'b'_{\alpha}}$ ($\mathrm{m^2\,s^{-3}}$) integrated over H_b for the $\Delta x = 1.5$ km case only, with spatial averages performed over the indicated areas.

d. *Restratification flux parameterizations*

Fox-Kemper et al. (2008) proposed a parameterization for restratification due to MLEs, under the assumption of a constant N^2 and $\nabla_h b_{\mathrm{ME}}$ over the mixed layer depth [similar to APE expression in (5)]. This is expressed in terms of an ageostrophic overturning eddy-induced streamfunction Φ^*, derived through a combination of model-based phenomenology and heuristics in the form

$$\Phi^* \sim C_{\mathrm{MLE}} \frac{H_b^2 \partial_x b_{\mathrm{ME}}}{f}, \tag{14}$$

where x is the cross-front direction, and C_{MLE} is an empirical constant. In the mixed layer the VBF can be written in terms of Φ^* as (Colas et al. 2013; Held and Schneider 1999),

$$\overline{w'b'_{\mathrm{MLE}}} \sim \Phi^* |\nabla_h b_{\mathrm{ME}}| \sim C_{\mathrm{MLE}} \frac{H_b^2 |\nabla_h b_{\mathrm{ME}}|}{f}. \tag{15}$$

Here, we have assumed that the cross-frontal gradient dominates $|\nabla_h b_{\mathrm{ME}}|$, that is, $\partial_x b_{\mathrm{ME}} \gg \partial_y b_{\mathrm{ME}}$. Equation (15) has been tested in realistic model configurations (Mensa et al. 2013; Luo et al. 2016) with some success but with caveats about the choice of C_{MLE}. Fox-Kemper et al. (2008) diagnoses the value of C_{MLE} in an idealized frontal spindown problem and finds $C_{\mathrm{MLE}} = 0.06$. Bachman and Taylor (2016) use equilibrated model cases of an idealized horizontal buoyancy gradient in the presence of mixing and suggest $O(1)$ values for the constant. Our value for the best fit shown in Fig. 20 is $C_{\mathrm{MLE}} = 0.3$, which is closer to the Bachman and Taylor (2016) estimate.

Mesoscale eddies can themselves generate fronts in the surface mixed layer, although their strain-induced frontogenesis occurs when a mesoscale strain field enhances a favorably aligned $\nabla_h b_{\mathrm{ME}}$ through an ageostrophic secondary circulation $(u, w) = (-\Phi_z, \Phi_x)$, with Φ as the associated overturning streamfunction. For a given mesoscale strain field α, where $\alpha^2 = (u_x + v_y)^2 + (u_y - v_x)^2$, the overturning streamfunction for a front takes the form

$$\Phi \sim -\frac{\alpha H_b^2 |\nabla_h b_{\mathrm{ME}}|}{f^2}. \tag{16}$$

The corresponding restratification flux averaged over many such fronts is

$$\overline{w'b'_{\alpha}} \sim C_{\alpha} \frac{\alpha H_b^2 |\nabla_h b_{\mathrm{ME}}|^2}{f^2}, \tag{17}$$

where the best-fit estimate for the southwestern Pacific region was $C_{\alpha} = 2.5$, which is consistent with the $O(1)$ value suggested by McWilliams (2016) in an idealized model of a front and a dense filament.

TTW fronts and filaments form under conditions of strong vertical mixing produced by a surface wind stress, in which case the lowest-order balance in the surface layer is no longer geostrophy but

$$f\mathbf{k} \times \mathbf{u}_h = -\nabla_h \phi + \partial_z (\nu_v \partial_z \phi), \quad \partial_z \phi = b. \tag{18}$$

Under such conditions nonzero values of $\mathbf{k} \times \nabla_h b$ can be enhanced by an emergent ageostrophic secondary circulation, which leads to fronts and filaments similar in structure to those seen in ''normal'' frontogenesis. In this case, the scaling for the overturning streamfunction takes the form (McWilliams 2016, manuscript submitted to *J. Fluid Mech.*)

$$\Phi \sim -\frac{\nu_v |\nabla_h b_{\mathrm{ME}}|}{f^2}. \tag{19}$$

Writing the eddy viscosity based on mixing length arguments or KPP as $\nu_v = u^* H_b$, we can write the restratification flux in the form of

$$\overline{w'b'_{\mathrm{TTW}}} \sim C_{\mathrm{TTW}} \frac{u^* H_b |\nabla_h b_{\mathrm{ME}}|^2}{f^2}, \tag{20}$$

where the best-fit estimate for C_{TTW} in this region is $C_{\mathrm{TTW}} = 0.07$, which is close to the $\approx$0.1 value found in the nonlinear TTW-front solutions by McWilliams (2016).

There is a striking similarity in the forms of the three restratification expressions (15), (17), and (20). In fact, all three dynamical processes extract energy from the common APE reservoir derived in (5). Depending on the relative strengths of α, u^*, and the depth of mixed layer H_b, one or another process might dominate. Thus, during the summer when the ML is shallow and under weak wind forcing conditions, $\overline{w'b'_\alpha}$ might be relevant, while the other two might coexist in conditions of strong winds and surface cooling, like in the southwestern Pacific. Based on the discussion in section 4c, we might expect wind stress effects to be more important in the Coral Sea during June and cooling after. However, based purely on the scalings derived above, the attribution problem is a difficult one, owing to the similar manifestation of frontal features in the three cases. In Fig. 20, we match VBF values obtained from ROMS with the three scalings. The constants (one for each scaling) are chosen to match the three geographical regions. While all three scalings do reasonably in the Solomon and Coral Seas, there is a pronounced lag of about 2 months in the Gulf of Papua subdomain, which is likely related to the interplay of shallow mixed layers and strong surface fronts that was speculated on in sections 4a and 4b. Equation (20) implies that all three parameterizations can be reasonable fits for $\overline{w'b'}$, which relates to the similarity in their scalings and their primary energy source in surface layer APE. Consequently, attempts to attribute all restratification to MLEs (Mensa et al. 2013; Luo et al. 2016) are doubtful. While instructive, the derived scalings are insufficiently discriminating among the mixed layer SM processes, and thus other approaches must be used.

5. Topographic submesoscale wakes

It is indicated in section 3b(2) that the interaction of surface waters with the various island chains in and around the Bismarck and Solomon Seas is a significant source of SCVs. These SCVs are formed by a barotropic–centrifugal instability of vortical wakes through separation of bottom drag–generated shear layers (Molemaker et al. 2015). To characterize the flow–topographic interactions, we examine the energetics of the surface flow. Barotropic instabilities involve a transfer of energy from the background mean flow to the eddies. With a decomposition of the flow fields into mean and deviations as $\mathbf{u} = \overline{\mathbf{u}} + \mathbf{u}'$, where the bar represents a combination of spatial and temporal averages, the energy transfer from mean to eddy KE is written as (Dong and McWilliams 2007)

$$\mathrm{KmKe} = \mathrm{HRS} + \mathrm{VRS}, \tag{21}$$

where

$$\mathrm{HRS} \equiv -(\overline{u'u'}\overline{u}_x + \overline{u'v'}\overline{u}_y + \overline{v'v'}\overline{v}_y + \overline{u'v'}\overline{v}_x) \tag{22}$$

and

$$\mathrm{VRS} = -(\overline{v'w'}\overline{v}_z + \overline{u'w'}\overline{u}_z) \tag{23}$$

are the contributions from the horizontal and vertical Reynolds stresses to the mean to eddy transfer; KmKe $>$ 0 implies that energy is transferred from the mean to the eddies and vice versa. In general, topographic eddy generation can occur at both mesoscales and SMs with the eddy scales depending on the Rossby and Burger [Bu $= (NH/fL)^2$, where N is the local buoyancy frequency] numbers associated with the topographic obstacles themselves (Dong and McWilliams 2007). Figure 21 shows a spatial map of HRS at a depth of $z = -20$ m (which is well within the mixed layer in this region) over the month of June [thus the averaging operator (22) is a monthly average here]. Strong positive signals in the wakes of headlands and island wakes surrounding the Solomon and Bismarck Seas are seen. These patches of positive HRS (mean to eddy conversions) have narrow (cross flow) spatial structures of $<$20 km in width, indicating that the eddy generation due to barotropic conversions happens at the SMs. These are likely a consequence of the small island sizes and equatorial proximity as conjectured in section 3b. The HRS signals in the inland Solomon Sea and the Coral Sea (not shown) are considerably weaker, seen in the figure as faint "smudges" of mesoscale extent. Based on the visual patterns of HRS distribution in this region, we examine the seasonal cycle of the energy conversions in four topographic regions marked as (1)–(4) in Fig. 21. Following the analysis methodology in preceding sections, we spatially average the three-dimensional HRS, VRS, and VBF over the respective regions to view their seasonal cycles over the top 100 m. Figure 22 has the results and can be used to infer the nature of the SM generation in these regions. In region 1, along the north coast of Papua New Guinea, HRS $\sim$ 3VBF $\sim$ 10VRS in the winter months, which shows that barotropic instability is dominant, as seen in the HRS patterns in Fig. 21 primarily along topographic wakes. The winter peak in HRS is contemporaneous with the peak mass flow rate across the Vitiaz Strait (not shown). Further, we attribute the VBF signal as being due to mixed layer SM generation rather than mixed barotropic–baroclinic instability, mediated by topography. Regions 2 and 3, composed of the island chains on the eastern coast of the Solomon Sea, have HRS $\sim$ 2VBF $\sim$ 10VRS, whereas in the southwestern Solomon Sea, VBF is of greater

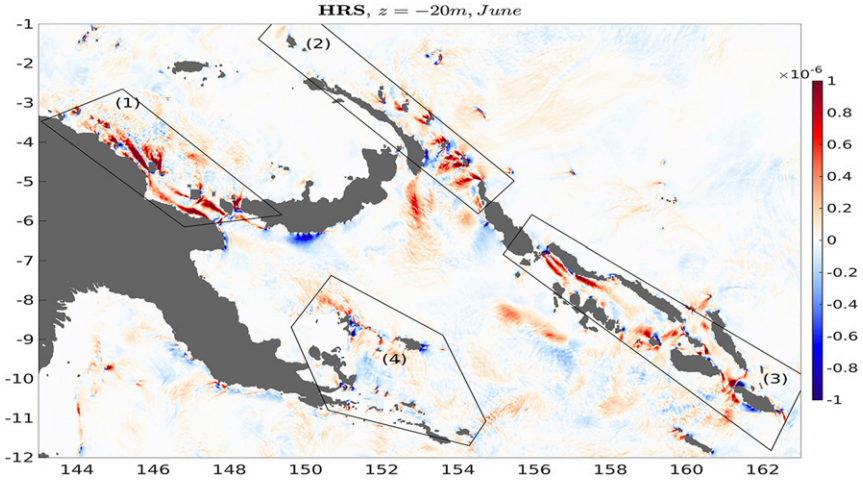

FIG. 21. HRS ($m^2 s^{-3}$) at $z = -20$ m averaged over the month of June for the topographically active region in and around the Solomon and Bismarck Seas. The four marked regions are the subject of further analysis in Fig. 22.

importance. Region 4, where the western boundary current traverses the Louisiade Archipelago at depth, does not have a strong SM generation signal, with only VRS a modest source in the surface layer. Thus, the strongest topographic generation happens along the Papua New Guinea coast, both relative to mixed layer SM processes and to other topographically complex regions surrounding the Solomon Sea.

It should be noted that the choice of the monthly averaging operator only identifies energy transfers from

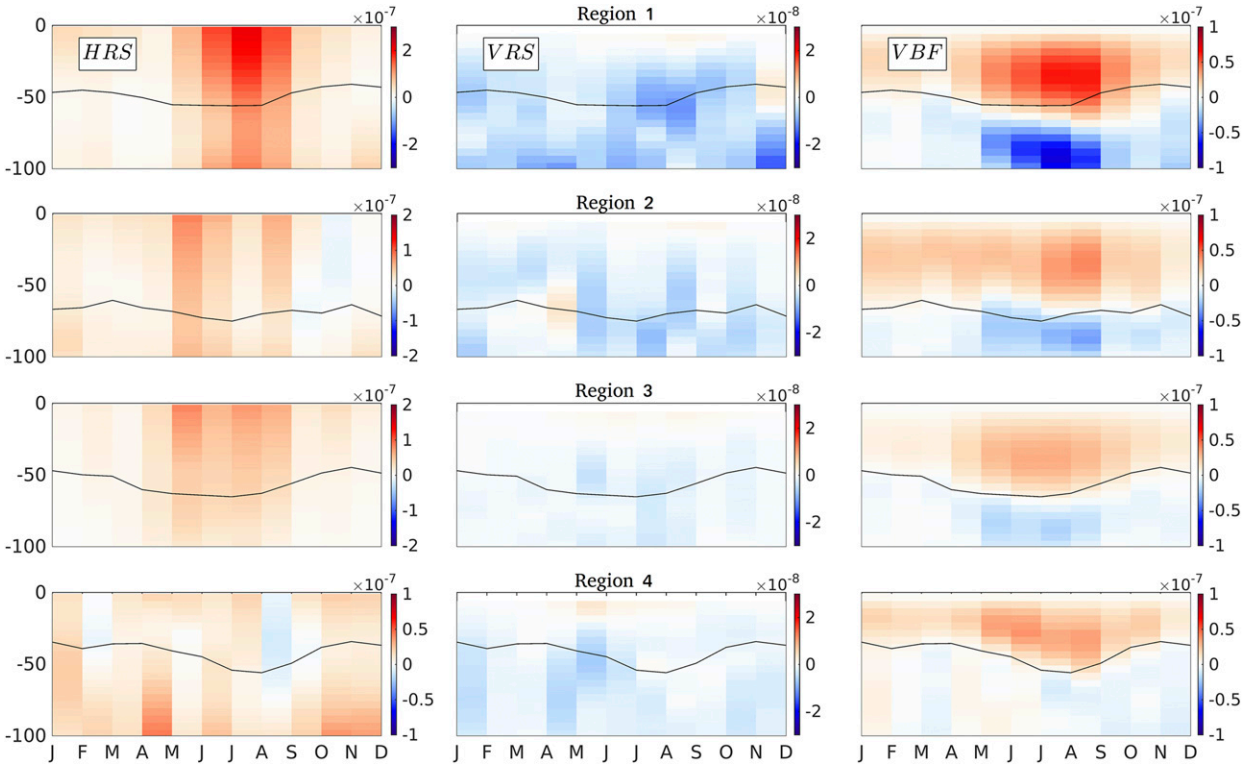

FIG. 22. Seasonal cycles of HRS, VRS, and VBF ($m^2 s^{-3}$) spatially averaged over the four regions marked in Fig. 21. Each row represents a region, with region 1 in Fig. 21, the first row, region 2 in the second row, and so on. Notice that the color bar ranges vary both among the rows and columns. The black curve in each plot shows the variation of H_b, spatially averaged over the respective region.

mean flows and mesoscale eddies with lifetimes longer than a month, and the transfer of energy from shorter-lived mesoscale eddies to SCVs would be unaccounted for.

6. Summary and conclusions

Surface layer submesoscale currents (SMs) are energized by a combination of nonlocal mesoscale eddy effects (through $\nabla_{\mathrm{ME}} b$ and α) and local forcings (τ and B_o) that generate surface layer APE [(5)] and vertical mixing. The APE reservoir can be accessed by any of the three mechanisms of TTW, MLEs, or strain-induced frontogenesis that are manifested through VBF, the conversion of mesoscale APE to frontal-scale KE, generating SMs and concomitantly restratifying the mixed layer. In the Coral Sea the restratification flux has a broad peak during the winter months of JJA. Because no significantly localized river sources of freshwater exist, a decomposition of the restratification flux into T and S components shows distinct peaks related to the months of maximum wind stress (seen in the vertical salinity flux) and surface cooling (seen in the vertical temperature flux). These two peaks are also seen in the seasonal cycle of frontal tendency. Equatorward of the Coral Sea, both the seasonal cycle and the peak value of B_o are weak, as are the corresponding restratification effects. The eastern Solomon Sea, in particular, is populated by large, R_d-size mesoscale eddies that are not conducive to SM frontogenesis, leading to a relative SM desert in this region year-round, clearly observed in the SM statistics of vorticity, surface divergence, and buoyancy gradient. Freshwater forcing at river mouths along the northern coast of Papua New Guinea and the western Solomon Sea generates fronts that contribute to the restratification flux and are comparable in magnitude to the VBF during the winter deepening. Restratification induced by freshwater fronts and mixed layer fronts, following the winter deepening, display distinct signatures in VSF and VTF, respectively. The largest riverine outflow in the region is in the Gulf of Papua, resulting in strong surface frontogenesis that matches the Coral Sea SM soup in intensity. However, there is only a weak restratification effect due to these freshwater fronts in the Gulf of Papua, possibly due to shallow mixed layers in the summer season when the river outflows peak. Shallow mixed layers reduce the APE reservoir and subsequently the restratification fluxes.

An important aspect of tropical oceans that has not been discussed here is the role of barrier layers on the SMs, that is, haloclines that limit the depth of surface layer vertical mixing. A recent study by Veneziani et al. (2014) focuses on boundary layers in the tropical North Atlantic and finds a close association with the formation, and in some cases the enhancement, of freshwater fronts. They find that the barrier layers have a small enhancement effect on the salinity restratification flux (VSF). Here, we have not examined the barrier layer dynamics in detail, partly because, unlike the North Atlantic, the topographic SMs in our region of interest dominate other effects and also because our climatological $E - P$ forcing might underestimate the effects of episodic high rain events. Flow–topographic interactions convert KE of the mean flow to KE in mesoscales and SMs, depending on the Rossby numbers associated with the topographic obstacles (Dong and McWilliams 2007). For large values of Ro, as is the case of the headlands and island chains around the near-equatorial ($f \rightarrow 0$) eastern and western coasts of the Bismarck Sea, the generation is largely in the SM range. These topography-induced SMs have weak restratification flux VBF, as also is seen in idealized (Dong and McWilliams 2007) and realistic midlatitude models (Gula et al. 2014), but they do have a strong signature in SM statistical measures of vertical velocity and vorticity variance. Moreover, the conversion of kinetic energy from the mean to eddies by horizontal Reynolds stress HRS is larger than that due to the vertical Reynolds stress VRS (which is negligible at the SM) or the vertical buoyancy flux VBF, indicating a dominant barotropic instability mechanism. North of the Vitiaz Strait, along the coast of Papua New Guinea, the HRS terms are about 3 times larger than the VBF, while along the Solomon Islands, they are larger by about a factor of 2. Furthermore, the HRS conversion primarily generates SCVs in these regions.

A key observation in this paper is that in spite of their near-coastal localization, topography-induced submesoscales can be, on average, stronger than those induced through mixed layer instabilities, evident from the zonally averaged statistics presented in Fig. 11. The dynamical consequences of this result remain to be explored. A possible effect is transfer of energy to smaller scales through three-dimensional centrifugal instability (CI), a form of negative potential vorticity instability. Molemaker et al. (2015) showed enhanced local dissipation in the California Undercurrent as it separates off a headland and generates anticyclonic SCVs, suggesting a CI-induced forward cascade (Dewar et al. 2015; Jiao and Dewar 2015). This is likely to be of particular importance in the Bismarck and Solomon Seas, where anticyclones with large vortex Rossby number Ro ~ 10 are commonplace [see section 3b(2)]. The $\Delta x = 500$ m and subsequently planned higher-resolution runs are likely to shed greater light on these phenomena.

Acknowledgments. This work was funded by NASA Grant NNX13AP51G and NSF Grant OCE-1419450.

REFERENCES

Bachman, S. D., and J. R. Taylor, 2016: Numerical simulations of the equilibrium between eddy-induced restratification and vertical mixing. *J. Phys. Oceanogr.*, **46**, 919–935, doi:10.1175/JPO-D-15-0110.1.

Boccaletti, G., R. Ferrari, and B. Fox-Kemper, 2007: Mixed layer instabilities and restratification. *J. Phys. Oceanogr.*, **37**, 2228–2250, doi:10.1175/JPO3101.1.

Brannigan, L., D. P. Marshall, A. Naveira-Garabato, and A. G. Nurser, 2015: The seasonal cycle of submesoscale flows. *Ocean Modell.*, **92**, 69–84, doi:10.1016/j.ocemod.2015.05.002.

Callies, J., R. Ferrari, J. M. Klymak, and J. Gula, 2015: Seasonality in submesoscale turbulence. *Nat. Commun.*, **6**, 6862, doi:10.1038/ncomms7862.

Capet, X., J. C. McWilliams, M. J. Molemaker, and A. F. Shchepetkin, 2008a: Mesoscale to submesoscale transition in the California Current System. Part I: Flow structure, eddy flux, and observational tests. *J. Phys. Oceanogr.*, **38**, 29–43, doi:10.1175/2007JPO3671.1.

——, ——, ——, and ——, 2008b: Mesoscale to submesoscale transition in the California Current System. Part II: Frontal processes. *J. Phys. Oceanogr.*, **38**, 44–64, doi:10.1175/2007JPO3672.1.

Carton, J. A., and B. S. Giese, 2008: A reanalysis of ocean climate using Simple Ocean Data Assimilation (SODA). *Mon. Wea. Rev.*, **136**, 2999–3017, doi:10.1175/2007MWR1978.1.

Chavanne, C. P., and P. Klein, 2016: Quasigeostrophic diagnosis of mixed layer dynamics embedded in a mesoscale turbulent field. *J. Phys. Oceanogr.*, **46**, 275–287, doi:10.1175/JPO-D-14-0178.1.

Chelton, D. B., M. G. Schlax, and R. M. Samelson, 2011: Global observations of nonlinear mesoscale eddies. *Prog. Oceanogr.*, **91**, 167–216, doi:10.1016/j.pocean.2011.01.002.

Colas, F., X. Capet, J. C. McWilliams, and Z. Li, 2013: Mesoscale eddy buoyancy flux and eddy-induced circulation in eastern boundary currents. *J. Phys. Oceanogr.*, **43**, 1073–1095, doi:10.1175/JPO-D-11-0241.1.

Couvelard, X., P. Marchesiello, L. Gourdeau, and J. Lefèvre, 2008: Barotropic zonal jets induced by islands in the southwest Pacific. *J. Phys. Oceanogr.*, **38**, 2185–2204, doi:10.1175/2008JPO3903.1.

——, F. Dumas, V. Garnier, A. Ponte, C. Talandier, and A. Treguier, 2015: Mixed layer formation and restratification in presence of mesoscale and submesoscale turbulence. *Ocean Modell.*, **96**, 243–253, doi:10.1016/j.ocemod.2015.10.004.

Danabasoglu, G., W. G. Large, J. J. Tribbia, P. R. Gent, B. P. Briegleb, and J. C. McWilliams, 2006: Diurnal coupling in the tropical oceans of CCSM3. *J. Climate*, **19**, 2347–2365, doi:10.1175/JCLI3739.1.

Dewar, W., J. McWilliams, and M. Molemaker, 2015: Centrifugal instability and mixing in the California Undercurrent. *J. Phys. Oceanogr.*, **45**, 1224–1241, doi:10.1175/JPO-D-13-0269.1.

Djath, B., J. Verron, A. Melet, L. Gourdeau, B. Barnier, and J.-M. Molines, 2014: Multiscale dynamical analysis of a high-resolution numerical model simulation of the Solomon Sea circulation. *J. Geophys. Res. Oceans*, **119**, 6286–6304, doi:10.1002/2013JC009695.

Dong, C., and J. C. McWilliams, 2007: A numerical study of island wakes in the Southern California Bight. *Cont. Shelf Res.*, **27**, 1233–1248, doi:10.1016/j.csr.2007.01.016.

Fox-Kemper, B., R. Ferrari, and R. Hallberg, 2008: Parameterization of mixed layer eddies. Part I: Theory and diagnosis. *J. Phys. Oceanogr.*, **38**, 1145–1165, doi:10.1175/2007JPO3792.1.

Gourdeau, L., J. Verron, A. Melet, W. Kessler, F. Marin, and B. Djath, 2014: Exploring the mesoscale activity in the Solomon Sea: A complementary approach with a numerical model and altimetric data. *J. Geophys. Res. Oceans*, **119**, 2290–2311, doi:10.1002/2013JC009614.

Gula, J., M. J. Molemaker, and J. C. McWilliams, 2014: Submesoscale cold filaments in the Gulf Stream. *J. Phys. Oceanogr.*, **44**, 2617–2643, doi:10.1175/JPO-D-14-0029.1.

——, ——, and ——, 2015: Topographic vorticity generation, submesoscale instability and vortex street formation in the Gulf Stream. *Geophys. Res. Lett.*, **42**, 4054–4062, doi:10.1002/2015GL063731.

Held, I. M., and T. Schneider, 1999: The surface branch of the zonally averaged mass transport circulation in the troposphere. *J. Atmos. Sci.*, **56**, 1688–1697, doi:10.1175/1520-0469(1999)056<1688:TSBOTZ>2.0.CO;2.

Hoskins, B. J., and F. P. Bretherton, 1972: Atmospheric frontogenesis models: Mathematical formulation and solution. *J. Atmos. Sci.*, **29**, 11–37, doi:10.1175/1520-0469(1972)029<0011:AFMMFA>2.0.CO;2.

Hristova, H. G., W. S. Kessler, J. C. McWilliams, and M. J. Molemaker, 2014: Mesoscale variability and its seasonality in the Solomon and Coral Seas. *J. Geophys. Res. Oceans*, **119**, 4669–4687, doi:10.1002/2013JC009741.

Jiao, Y., and W. Dewar, 2015: The energetics of centrifugal instability. *J. Phys. Oceanogr.*, **45**, 1554–1573, doi:10.1175/JPO-D-14-0064.1.

Kessler, W. S., and S. Cravatte, 2013: ENSO and short-term variability of the South Equatorial Current entering the Coral Sea. *J. Phys. Oceanogr.*, **43**, 956–969, doi:10.1175/JPO-D-12-0113.1.

Large, W., J. C. McWilliams, and S. C. Doney, 1994: Oceanic vertical mixing: A review and a model with a nonlocal boundary layer parameterization. *Rev. Geophys.*, **32**, 363–403, doi:10.1029/94RG01872.

Lemarié, F., J. Kurian, A. F. Shchepetkin, M. J. Molemaker, F. Colas, and J. C. McWilliams, 2012: Are there inescapable issues prohibiting the use of terrain-following coordinates in climate models? *Ocean Modell.*, **42**, 57–79, doi:10.1016/j.ocemod.2011.11.007.

Luo, H., A. Bracco, Y. Cardona, and J. C. McWilliams, 2016: Submesoscale circulation in the northern Gulf of Mexico: Surface processes and the impact of the freshwater river input. *Ocean Modell.*, **101**, 68–82, doi:10.1016/j.ocemod.2016.03.003.

Mason, E., M. J. Molemaker, A. Shchepetkin, F. Colas, J. C. McWilliams, and P. Sangrà, 2010: Procedures for offline grid nesting in regional ocean models. *Ocean Modell.*, **35**, 1–15, doi:10.1016/j.ocemod.2010.05.007.

McWilliams, J. C., 1985: Submesoscale, coherent vortices in the ocean. *Rev. Geophys.*, **23**, 165–182, doi:10.1029/RG023i002p00165.

——, 2016: Submesoscale currents in the ocean. *Proc. Roy. Soc.*, **A472**, 20160117, doi:10.1098/rspa.2016.0117.

——, and E. Huckle, 2006: Ekman layer rectification. *J. Phys. Oceanogr.*, **36**, 1646–1659, doi:10.1175/JPO2912.1.

——, ——, and A. F. Shchepetkin, 2009: Effects in a stratified Ekman layer. *J. Phys. Oceanogr.*, **39**, 2581–2599, doi:10.1175/2009JPO4130.1.

——, J. Gula, M. J. Molemaker, L. Renault, and A. F. Shchepetkin, 2015: Filament frontogenesis by boundary layer turbulence. *J. Phys. Oceanogr.*, **45**, 1988–2005, doi:10.1175/JPO-D-14-0211.1.

Melet, A., L. Gourdeau, and J. Verron, 2010: Variability in Solomon Sea circulation derived from altimeter sea level data. *Ocean Dyn.*, **60**, 883–900, doi:10.1007/s10236-010-0302-6.

Mensa, J. A., Z. Garraffo, A. Griffa, T. M. Özgökmen, A. Haza, and M. Veneziani, 2013: Seasonality of the submesoscale dynamics in the Gulf Stream region. *Ocean Dyn.*, **63**, 923–941, doi:10.1007/s10236-013-0633-1.

Molemaker, M. J., J. C. McWilliams, and W. K. Dewar, 2015: Submesoscale instability and generation of mesoscale anticyclones near a separation of the California Undercurrent. *J. Phys. Oceanogr.*, **45**, 613–629, doi:10.1175/JPO-D-13-0225.1.

Nagai, T., A. Tandon, and D. Rudnick, 2006: Two-dimensional ageostrophic secondary circulation at ocean fronts due to vertical mixing and large-scale deformation. *J. Geophys. Res.*, **111**, C09038, doi:10.1029/2005JC002964.

Qiu, B., S. Chen, and W. S. Kessler, 2009: Source of the 70-day mesoscale eddy variability in the Coral Sea and the North Fiji Basin. *J. Phys. Oceanogr.*, **39**, 404–420, doi:10.1175/2008JPO3988.1.

Shchepetkin, A. F., and J. C. McWilliams, 2003: A method for computing horizontal pressure-gradient force in an oceanic model with a nonaligned vertical coordinate. *J. Geophys. Res.*, **108**, 3090, doi:10.1029/2001JC001047.

——, and ——, 2005: The Regional Oceanic Modeling System (ROMS): A split-explicit, free-surface, topography-following-coordinate oceanic model. *Ocean Modell.*, **9**, 347–404, doi:10.1016/j.ocemod.2004.08.002.

——, and ——, 2009: Correction and commentary for ''Ocean forecasting in terrain-following coordinates: Formulation and skill assessment of the regional ocean modeling system'' by Haidvogel et al., J. Comp. Phys. 277, pp. 3595–3624. *J. Comput. Phys.*, **228**, 8985–9000, doi:10.1016/j.jcp.2009.09.002.

Stammer, D., 1997: Global characteristics of ocean variability estimated from regional TOPEX/POSEIDON altimeter measurements. *J. Phys. Oceanogr.*, **27**, 1743–1769, doi:10.1175/1520-0485(1997)027<1743:GCOOVE>2.0.CO;2.

Tulloch, R., J. Marshall, C. Hill, and K. S. Smith, 2011: Scales, growth rates, and spectral fluxes of baroclinic instability in the ocean. *J. Phys. Oceanogr.*, **41**, 1057–1076, doi:10.1175/2011JPO4404.1.

Veneziani, M., A. Griffa, Z. Garraffo, and J. A. Mensa, 2014: Barrier layers in the tropical South Atlantic: Mean dynamics and submesoscale effects. *J. Phys. Oceanogr.*, **44**, 265–288, doi:10.1175/JPO-D-13-064.1.